Journal of Zhejiang University-SCIENCE B (Biomedicine & Biotechnology) in press
www.jzus.zju.edu.cn; www.springer.com/journal/11585
E-mail: jzus_b@zju.edu.cn

Research Article

https://doi.org/10.1631/jzus.B2500567

TAF1 aggravates ferroptosis by promoting ubiquitin-mediated degradation of nGPX4

Kehong YE[1,2], Meifu GAN[3], Liang SUN[1], Chaoyi CHEN[4], Xuan LAI[1], Yinjun HE[5], Ming ZHU[1], Weiqin JIANG[6]✉, Honghe ZHANG[1]✉

[1]*Department of Pathology, Zhejiang University School of Medicine, Hangzhou 310058, China*
[2]*Department of Pathology, Zhejiang Cancer Hospital, Hangzhou Institute of Medicine (HIM), Chinese Academy of Sciences, Hangzhou 310011, China*
[3]*Taizhou Hospital of Zhejiang Province affiliated to Wenzhou Medical University, Taizhou 317000, China*
[4]*Department of Colorectal Surgery and Oncology (Key Laboratory of Cancer Prevention and Intervention, China National Ministry of Education, Key Laboratory of Molecular Biology in Medical Sciences, Zhejiang Province, China), The Second Affiliated Hospital, Zhejiang University School of Medicine, Hangzhou 310009, China*
[5]*Department of Pathology, State Key Laboratory of Complex Severe and Rare Disease, Molecular Pathology Research Center, Peking Union Medical College Hospital, Chinese Academy of Medical Sciences and Peking Union Medical College, Beijing 100730, China*
[6]*Department of Colorectal Surgery and Oncology, The First Affiliated Hospital, Zhejiang University School of Medicine, Hangzhou 310006, China*

Unedited

Highlights

- TAF1 inhibits ferroptosis via the p53/SLC7A11 axis in p53-wild-type cells.
- TAF1 promotes ferroptosis through proteasomal degradation of nuclear GPX4 in p53-mutant cells.
- TAF1 facilitates K11-linked ubiquitination and proteasomal degradation of nuclear GPX4.

Abstract: Glutathione peroxidase 4 (GPX4) is a primary inhibitor of ferroptosis, a regulated form of cell death driven by the accumulation of lipid hydroperoxides. GPX4 exists in three isoforms localized in the cytosol, mitochondria and nucleus, respectively; however, the regulatory mechanisms governing nuclear GPX4 (nGPX4) remain largely unclear. Herein, we identified TATA-box binding protein-associated factor 1 (TAF1) as a pivotal regulator of nGPX4. TAF1 phosphorylates nGPX4, leading to its K11-linked ubiquitination and proteasomal degradation, thereby promoting ferroptosis in p53-mutant cells. Conversely, in p53-wild-type cells, TAF1 phosphorylates p53, facilitating MDM2 proto-oncogene (MDM2)-mediated p53 degradation, which upregulates solute carrier family 7 member 11 (SLC7A11) expression and reduces cellular susceptibility to ferroptosis. Collectively, TAF1 plays dual and context-dependent roles in ferroptosis regulation, acting as both a promoter and inhibitor depending on the p53 status.

Key words: TATA-box binding protein-associated factor 1 (TAF1); p53; Ferroptosis; Glutathione peroxidase 4 (GPX4); Protein degradation

1 Introduction

TAF1, the largest subunit of the general transcription factor TFIID (Wang et al., 2014) is a key component

✉ Honghe ZHANG, honghezhang@zju.edu.cn
Weiqin JIANG, weiqinjiang@zju.edu.cn
Honghe ZHANG, https://orcid.org/0000-0001-5954-2857
Weiqin JIANG, https://orcid.org/0000-0003-3200-8835
Kehong YE, https://orcid.org/0000-0002-3364-7850

Received Sept. 8, 2025; Revision accepted Nov. 11, 2025;
Crosschecked xxx. xx, 20xx; Published online xxx. xx, 20xx

© Zhejiang University Press 2025

of the RNA polymerase II transcription machinery and has been implicated in several neurodegenerative disorders, including X-linked dystonia–parkinsonism (XDP) (Aneichyk et al., 2018), X-linked syndromic mental retardation-33 (MRXS33) (Cheng et al., 2020), and TAF1 intellectual disability syndrome (TAF1 ID syndrome) (Janakiraman et al., 2020). Beyond its role in neurodegeneration, TAF1 also participates in tumorigenesis and cancer progression. Elevated TAF1 expression has been reported in various tumor types (Zhou et al., 2021), and TAF1 mutations have been associated with gastric, colorectal and ovarian cancers (Ribeiro et al., 2014; Oh et al., 2017) Notably, such mutations occur more frequently in peritoneal carcinomatosis than in primary gastric adenocarcinoma (Wang et al., 2020), suggesting the potential role of TAF1 in promoting metastatic dissemination. Structurally, TAF1 comprises an N-terminal kinase domain, a C-terminal kinase domain (Dikstein et al., 1996), a histone acetyltransferase domain (Mizzen et al., 1996), and an E1/E2 ubiquitin-activating/conjugating domain (Pham, 2000), each conferring distinct regulatory functions in cancer biology (Tavassoli et al., 2010; Xu et al., 2019).

Ferroptosis, a recently discovered form of regulated cell death, is driven by the accumulation of iron-dependent phospholipid hydroperoxides (Dixon et al., 2012). These are generated either through lipoxygenase activity or by reactive oxygen species (ROS) derived from membrane electron transport proteins attacking polyunsaturated fatty acids (PUFAs) (Chen et al., 2021). The detoxification of phospholipid hydroperoxides depends on several antioxidant systems, including the SLC7A11-glutathione(GSH)-GPX4 pathway (Dixon et al., 2014; Yang et al., 2014) the coenzyme Q10 (CoQ10)-ferroptosis suppressor protein 1 (FSP1) pathway (Doll et al., 2019), and the CoQ10-dihydroorotate dehydrogenase (DHODH) pathway (Mao et al., 2021). Among these, the most extensively studied pathway is SLC7A11-GSH-GPX4. At the core of this pathway is GPX4, a selenoprotein (Yang et al., 2016; Xie et al., 2023) that utilizes GSH to reduce lipid peroxides to their corresponding alcohols (Yang, et al., 2014). GPX4 exists in three isoforms—cytoplasmic (cGPX4), mitochondrial (mGPX4), and nuclear (nGPX4). While the functions and regulatory mechanisms of cGPX4 and mGPX4 have been well characterized (Deng et al., 2021; Qian et al., 2023; Guo et al., 2024; Xie et al., 2024), those of nGPX4 remain poorly understood.

In this study, we identified TAF1 as a critical regulator of ferroptosis whose function depends on the p53 status. In p53-wild-type cells, TAF1 alleviates ferroptosis by promoting p53 degradation, thereby upregulating SLC7A11 expression. In contrast, in p53-mutant cells, TAF1 promotes ferroptosis by facilitating the K11-linked ubiquitination and proteasomal degradation of nGPX4. These findings uncover a previously unrecognized mechanism linking TAF1 to ferroptosis regulation.

Unedited

2 Methods and materials

2.1 Analysis of public datasets

Total RNA expression profiling data from 12 ovarian cancer (OV) patients and 57 healthy donors were obtained from the GSE66957 dataset available in the Gene Expression Omnibus (GEO) database. In addition, The Cancer Genome Atlas (TCGA) ovarian cancer dataset and colon adenocarcinoma (COAD) dataset were retrieved from the UCSC Xena platform (https://xenabrowser.net/).

2.2 Cell culture

The colorectal cancer cell lines RKO and SW620 were obtained from the American Type Culture Collection (ATCC, Manassas, VA, USA). The ovarian cancer cell lines SKOV3 and A2780 were kindly provided by Dr. Yihua WU (Zhejiang University School of Medicine, Hangzhou, China). The human embryonic kidney 293T (HEK293T) cells were purchased from the Cell Bank of the Chinese Academy of Sciences (Shanghai, China). The normal human colonic epithelial cell line NCM460 was obtained from EK-Bioscience (Shanghai, China).

The RKO, SKOV3, A2780, and HEK293T cells were cultured in Dulbecco's Modified Eagle Medium

(DMEM) (Gibco, NY, USA), while SW620 and NCM460 cells were cultured in Roswell Park Memorial Institute (RPMI) 1640 medium (Gibco, NY, USA). All media were supplemented with 10% (volume fraction) fetal bovine serum (FBS) (C04001-500, Vivacell, Shanghai, China) and 1% (volume fraction) penicillin/streptomycin (BL505A, Biosharp, Hefei, China). Cells were dissociated using 0.03% trypsin containing EDTA and maintained in a cell culture incubator at 37 °C with 5% CO_2. Plasmids were transfected into colorectal cancer (CRC) and OV cell lines using the Neofect™ DNA transfection reagent kit (TF201201, Neofect, Beijing, China) following the manufacturer's protocol, while HEK293T cells were transfected using LipoD293 (SL100668, SignaGen, Changzhou, China).

2.3 Generation of TAF1 knockout cells

In order to generate TAF1 knockout cells, the pLentiCRISPR v2-TAF1 plasmid was co-transfected with two lentiviral packaging plasmids, psPAX2 and pMD2.G, into HEK293T cells using LipoD293 according to the manufacturer's instructions. After 48 h, the culture medium containing viral particles was collected and used to infect RKO, SW620, SKOV3, and A2780 cell lines for 24 h. Following infection, puromycin was added to the culture medium for selection. After two weeks of selection, surviving cells were individually plated into 96-well plates. These subclones were expanded and screened for TAF1 knockout by sequencing and immunoblotting, and cells that did not exhibit the knockout were considered Mock cells. The sgRNA sequences used for the knockout were listed in Table 1.

Table 1 Oligonucleotide sequences used in this study

Crispr gRNA sequences		
TAF1 sgRNA	CCGAAGATACCAGCAGACGA	Cas9
qPCR primer sequences		
Target	**F**	**R**
SLC7A11	GGACAAGAAACCCAGGTGGT	GCAGATTGCCAAGATCTCAAGT
GPX4	CAGTGAGGCAAGACCGAAGT	CCGAACTGGTTACACGGGAA
GAPDH	CCCTTCATTGACCTCAACTACATG	TGGGATTTCCATTGATGACAAGC

Unedited

2.4 Quantitative real-time PCR (qPCR)

Total RNA was extracted from the indicated cells using TRIzol (15596018, Invitrogen, CA, USA) according to the manufacturer's instructions. cDNA was synthesized using HiScript II reverse transcriptase (R223-01, Vazyme, Nanjing, China), followed by qPCR using SYBR qPCR Master Mix (Q711-02, Vazyme, Nanjing, China). The gene-specific primers used for amplification were listed in Table 1

2.5 Immunoblotting and immunoprecipitation

Cells were harvested and lysed in RIPA Lysis Buffer (P0013C, Beyotime, Shanghai, China) supplemented with PMSF (ST505, Beyotime, Shanghai, China) and a protease inhibitor cocktail (HY-K0010, MCE, NJ, USA). The lysates were sonicated on ice to ensure complete cell lysis and then centrifuged at 13,300 r/min for 10 min at 4 °C to collect the supernatant. The protein concentration was determined using the BCA assay (23225, Thermo Scientific, MA, USA).

Proteins were separated by SDS-PAGE, transferred to nitrocellulose membranes (HATF00010, Merck Millipore, MA, USA), and blocked with 50g/L skimmed milk. Membranes were incubated overnight at 4 °C with primary antibodies. After 1 h of incubation with secondary antibodies at room temperature, protein signals were detected using the Odyssey Imaging System (LI-COR, NE, USA).

For the immunoprecipitation (IP) of exogenously expressed FLAG-tagged, HA-tagged, or GFP-tagged

proteins, cells were harvested 48 h post-transfection and lysed in IP Lysis Buffer (P0013J, Beyotime, Shanghai, China), supplemented with PMSF and protease inhibitor cocktail. The lysates were sonicated, centrifuged at 13,300 r/min for 10 min at 4 °C to obtain the supernatant, and then incubated overnight at 4 °C with Anti-FLAG M2 Magnetic Beads (M8823, Sigma, MO, USA) or Anti-HA Magnetic Beads (SAE0197, Sigma, MO, USA) in a rotating incubator. The immunoprecipitates were washed several times with TBS (ST661, Beyotime, Shanghai, China) and analyzed by western blotting.

To detect the ubiquitination of FLAG-tagged GPX4, cells were transfected for 48 h and then treated with MG132 (10 μmol/L; HY-13259, MCE, NJ, USA) for 4 h. Cells were then lysed in RIPA Lysis Buffer supplemented with PMSF and protease inhibitor cocktail. The lysates were incubated overnight at 4 °C with Anti-FLAG M2 Magnetic Beads. Afterwards, the beads were washed several times with TBS and analyzed by western blotting.

All immunoblotting (IB) and immunoprecipitation (IP) experiments were performed independently at least three times, and the representative results are shown. Protein decay curves are presented as the mean ± standard deviation (SD). of three independent experiments. The plasmids and antibodies used in this study were listed in Table 2 and Table 3, respectively.

Unedited

Table 2 Plasmids used in this study

Plasmid name	Vector	Application
TAF1 KO sgRNA	pLentiv-V2	CRISPR/Cas9
GFP-TAF1	pCS2+	Overexpression and IP
Flag-TAF1	pCDNA3.1	Overexpression and IP
Flag-GPX4	pCDNA3.1	Overexpression and IP
HA-GPX4	pCDH	Overexpression and IP
Flag-TBP	pCDNA3.1	Overexpression and IP
Flag-DUF	pCDNA3.1	Overexpression and IP
Flag-ZINC	pCDNA3.1	Overexpression and IP
Flag-BRD	pCDNA3.1	Overexpression and IP
HA-Ub	pCDNA3.1	Overexpression and IP
HA-UB-K6	pCDNA3.1	Overexpression and IP
HA-UB-K11	pCDNA3.1	Overexpression and IP
HA-UB-K27	pCDNA3.1	Overexpression and IP
HA-UB-K29	pCDNA3.1	Overexpression and IP
HA-UB-K33	pCDNA3.1	Overexpression and IP
HA-UB-K48	pCDNA3.1	Overexpression and IP
HA-UB-K63	pCDNA3.1	Overexpression and IP

Table 3 Antibodies used in this study

Target	Clone	Company	Catalog Number	Application
TAF1	Rabbit monoclonal	CST	12781S	WB
TAF1	Rabbit polyclonal	Proteintech	20260-1-AP	IHC
IREB2	Rabbit monoclonal	Abcam	ab181153	WB
ACSL4	Mouse monoclonal	Santa Cruz	sc-271800	WB
P53	Rabbit monoclonal	CST	2527T	WB
FTL	Rabbit monoclonal	Abcam	ab109373	WB
SLC3A2	Rabbit monoclonal	CST	47213S	WB
SLC7A11	Rabbit monoclonal	CST	12691S	WB
GPX4	Rabbit monoclonal	Abcam	ab125066	WB, IF and IHC
4-Hydroxynonenal	Rabbit polyclonal	Abcam	ab46545	IHC

NCOA4	Rabbit monoclonal	CST	66849S	WB
FSP1(AMID)	Mouse monoclonal	Santa Cruz	sc-376987	WB
FTH1	Rabbit monoclonal	CST	4393S	WB
DMT1	Rabbit monoclonal	CST	15083S	WB
GAPDH	Mouse monoclonal	Proteintech	60004-1-Ig	WB
GAPDH	Rabbit polyclonal	Proteintech	10494-1-AP	WB
Flag	Mouse monoclonal	Sigma Aldrich	F1804	WB
HA	Rabbit monoclonal	Abclonal	AE105	WB

Abcam (MA, USA); Abclonal (Wuhan, China); Cell signaling technology (CST; MA, USA); Proteintech (Wuhan, China); Santa Cruz (CA, USA); Sigma Aldrich (MO, USA).

2.6 RNA-seq and enrichment analysis

The PolyA-RNA of SKOV3-Mock and SKOV3-KO cells treated with DMSO, RSL3 and RSL3+Ferrostatn-1 was extracted, sequenced and analyzed by Bioacme (Wuhan, China). Three biological replicates were used for each condition. The individual RNA seq libraries were pooled based on their respective sample specific-6 bp adaptors and sequenced at 150 bp/sequence pair-read using an Illumina NovaSeq system. Reads were mapped into the hg19 reference genome by STAR (Dobin et al., 2013) and quantified by RSEM (Li and Dewey, 2011). Gene differential expression analysis was accomplished by the DESeq2 (Love et al., 2014) package in R. The Benjamini-Hochberg false discovery rate method was applied to correct for multiple hypothesis testing. The genes with adjust $p < 0.05$ and fold change >1 or <-1 were defined as differentially expressed genes (DEGs) and candidates for further analysis. Gene expression heatmap was accomplished with the R package heatmap. Gene Ontology (GO) enrichment analysis and Kyoto Encyclopedia of Genes and Genomes (KEGG) enrichment analysis were performed using the online tools DAVID (http://david.abcc.ncifcrf.gov). The results were visualized by the R package ggplot2 in R software.

Unedited

2.7 Immunofluorescence assay

Cells were gently washed three times with phosphate buffered saline (PBS) at 37 °C before fixation in 4% (volume fraction) paraformaldehyde for 20 min. After permeabilization with 0.5% (volume fraction) Triton X-100 for 10 min, cells were blocked with 10% (volume fraction) fetal bovine serum for 1 h at room temperature, then incubated with the primary antibody overnight at 4 °C in a humidified chamber. The following day, cells were incubated with an Alexa Fluor 546-conjugated anti-rabbit secondary antibody (A-11010, Invitrogen, CA, USA) for 1 h at room temperature in the dark. Nuclei were counterstained with 4',6-diamidino-2-phenylindole (DAPI) (C1002, Beyotime, Shanghai, China) for 20 min in PBS. Fluorescence signals were captured using high-resolution confocal microscopy (IX83-FV3000-OSR, Olympus, Tokyo, Japan). Representative images depicting the subcellular localization of each molecule are shown. All confocal analyses were performed in triplicate.

2.8 Cellular reactive oxygen species assay

In order to assess intracellular ROS levels, harvested cells were washed three times with serum-free culture media and then incubated with 2',7'-dichlorodihydrofluorescein diacetate (DCFH-DA) (S0033S, Beyotime, Shanghai, China) at 37 °C with 5% CO_2 in the dark for 20 min. Following incubation, cells were washed three additional times with serum-free culture media. The cell suspension was filtered through a 40 μm nylon mesh cell strainer and analyzed using a DxFLEX Flow Cytometer (Beckman, CA, USA).

To evaluate the effects of ferroptosis and other regulated cell death (RCD) inhibitors on ROS levels, cells were co-treated with RSL3 (S8155, Selleck, TX, USA) in combination with ferrostatin-1 (S7243, Selleck, TX, USA), Z-VAD-FMK (S7023, Selleck, TX, USA), Necrostatin-1 (S8037, Selleck, TX, USA), or chloroquine (HY-17589A, MCE, NJ, USA) for the indicated duration before ROS measurement.

2.9 Cell viability assay

Equal numbers of cells were seeded into 96-well plates and incubated with increasing concentrations of RSL3 for 48 h. Cell viability was assessed using the CCK8 kit (AR1160, Boster, Wuhan, China) according to the manufacturer's instructions. Absorbance at 450 nm was measured using a microplate reader.

2.10 Lipid peroxidation assay

Lipid peroxidation was assessed using BODIPY 581/591 C11 staining (S0043S, Beyotime, Shanghai, China). Cells were washed three times with PBS and incubated with 2 μmol/L BODIPY 581/591 C11 in PBS at 37°C for 30 min in a 5% CO_2 incubator. After staining, cells were washed three times with PBS and fluorescence signals were visualized using a confocal microscope (IX83-FV3000-OSR, Olympus, Tokyo, Japan). The shift in mean fluorescence intensity from the non-oxidized (red) to the oxidized (green) channel was quantified using ImageJ software.

2.11 Cellular Fe^{2+} assay

In order to assess the intracellular Fe^{2+} levels via fluorescence microscopy, cells were pre-seeded in glass-bottom cell culture dishes (801001, Nest, Wuxi, China) and incubated overnight at 37 °C in a 5% CO_2 incubator. The following day, the supernatant was carefully removed and cells were washed three times with HBSS (24020117, Gibco, NY, USA). A working solution of FerroOrange (1 μmol/L; F374, Dojindo, Tabaru, Japan) was then added and cells were incubated for 30 min at 37 °C in a 5% CO_2 incubator. Fluorescent signals were visualized using a high-resolution confocal microscope (IX83-FV3000-OSR, Olympus, Tokyo, Japan).

2.12 Mouse models

All animal experiments were conducted in accordance with protocols approved by the Institutional Animal Care and Use Committee of Zhejiang University (Ethics Committee number: ZJU20240161).

To evaluate whether TAF1 deletion affects the susceptibility of p53-mutant cells to ferroptosis in vivo, 4×10^6 SW620 TAF1-Mock or SW620 TAF1-KO cells were subcutaneously injected into nude mice (male, 5 weeks old). When the tumor volumes reached 50 mm3, mice were administered intraperitoneal injections of either 250 μL vehicle (5% DMSO, 40% PEG300, 5% Tween-80, and 50% ddH_2O, volume fraction) or RSL3 (30 mg/kg in the same vehicle; S8155, Selleck, TX, USA) every other day. Tumor diameters were measured every other day and tumor volumes were calculated using the formula of length×width×width×0.5.

2.13 Histological analysis

Subcutaneous tumors in mice were fixed in 4% (volume fraction) paraformaldehyde for over 48 h and then paraffin-embedded. Tissue sections were cut to a thickness of 4 μm and subjected to hematoxylin and eosin (H&E) staining and immunohistochemistry. The sections were first dewaxed and rehydrated in xylene and graded ethanol, followed by incubation in 3% (volume fraction) hydrogen peroxide methanol to block endogenous peroxidase activity. Antigen retrieval was performed using citrate buffer (0.01 mol/L, pH 6.0), and tissues were blocked with 10% (volume fraction) normal goat serum for 30 min at room temperature. Sections were then incubated overnight with rabbit anti-TAF1 (1:600; 20260-1-AP, Proteintech, Wuhan, China), anti-GPX4 (1:100; ab125066, Abcam, MA, USA), or anti-4-Hydroxynonenal (1:100; ab46545, Abcam, MA, USA) at 4 °C in a humidified chamber. Afterwards, tissues were incubated with a secondary antibody for 30 min at room temperature. The tissues were developed using 3,3-diaminobenzidine (Zhongshan Golden Bridge Biotechnology, Beijing, China), counterstained with hematoxylin, and then dehydrated in graded alcohols. Finally, sections were mounted with coverslips and observed under a light microscope.

2.14 Quantifications and statistical analysis

All data are presented as mean± SD. Statistical comparisons between two groups were performed using Student's t-test for paired or independent samples. One-way ANOVA was used for comparisons among

Unedited

multiple groups. Kaplan-Meier survival analysis was conducted using IBM SPSS Statistics 20, with significance assessed by the log-rank test. A *P*-value of <0.05 was considered statistically significant. Significance levels are indicated as follows: $^{*}P<0.05$, $^{**}P<0.01$, $^{***}P<0.001$, and ns (not significant).

3 Results

3.1 TAF1 as a potential driver of ferroptosis

In order to identify potential ferroptosis drivers, we analyzed the National Cancer Institute Genomic Data Commons (GDC) Pan-Cancer dataset using the UCSC Xena Browser (https://xenabrowser.net/) (Goldman et al., 2020). This analysis revealed that the mRNA expression levels of 177 genes were negatively correlated with four canonical ferroptosis suppressors, including GPX4, FSP1 (Bersuker et al., 2019), ferritin light chain (FTL) and ferritin heavy chain 1 (FTH1) (Hou et al., 2016) (Fig. 1a). Several of these genes have been previously implicated in apoptosis or necroptosis, such as never in mitosis gene A-related kinase 1 (NEK1) (Spies et al., 2016; Wang et al., 2021), ATRX chromatin remodeler (ATRX) (Wang et al., 2024), and YTH N6-methyladenosine RNA binding protein C1 (YTHDC1) (Feng et al., 2024).

Unedited

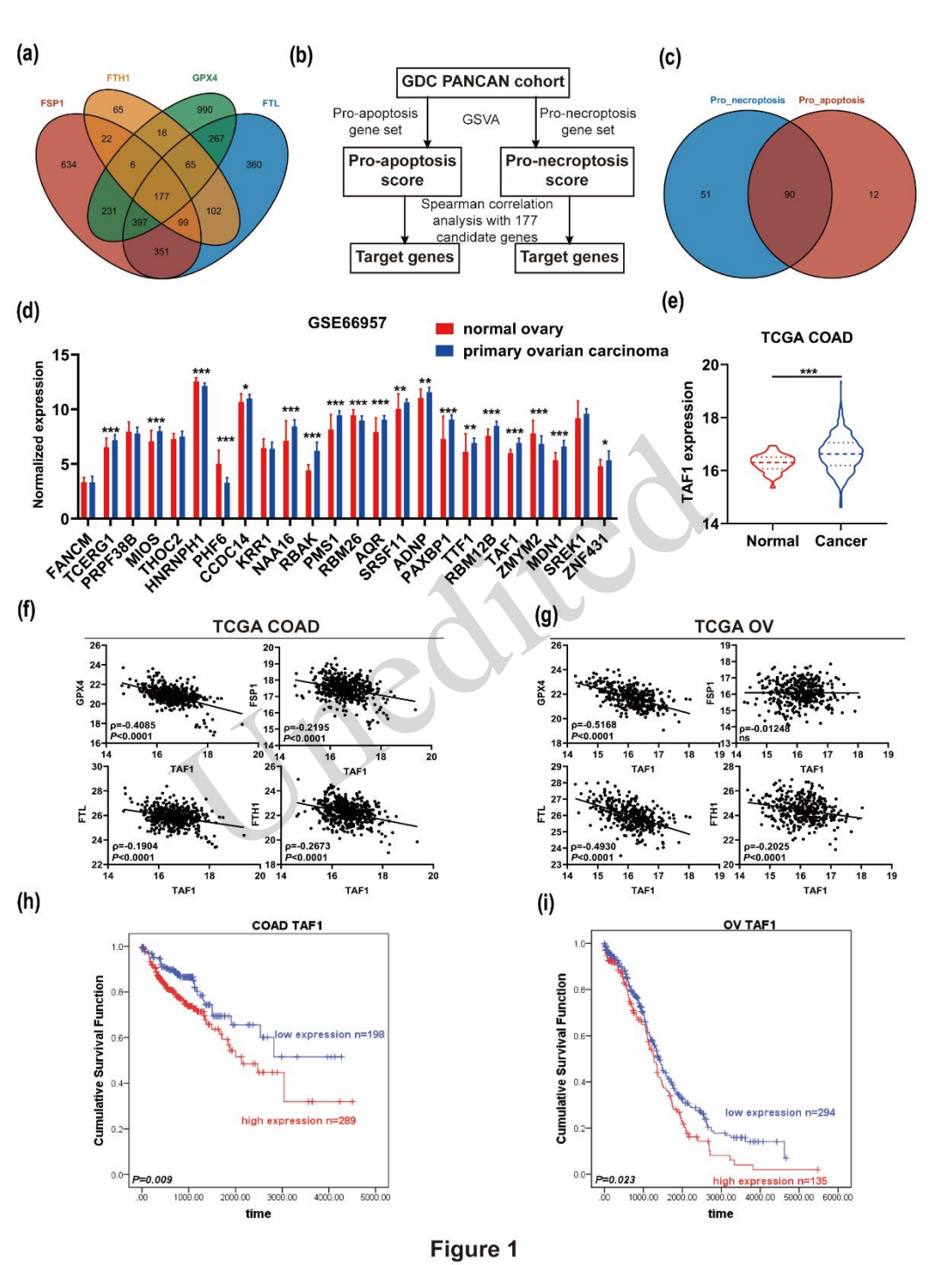

Figure 1

Fig. 1 TAF1 as a potential driver of ferroptosis.

(a) Venn diagram showing the numbers of genes whose mRNA expression levels were negatively correlated with those of GPX4, FSP1, FTH1, and FTL (P<0.00001, ρ< -0.23). (b) Schematic representation of the screening strategy used to identify genes associated with apoptosis and necroptosis. (c) Venn diagram showing the numbers of genes that were not correlated with apoptosis or necroptosis (|ρ|<0.2). (d) Analysis of the mRNA expression levels of 27 candidate genes in ovarian serous cystadenocarcinoma tissues (n = 57) and normal ovarian tissues (n=12) from the GSE66957 dataset. (e) Analysis of TAF1 mRNA levels in colon adenocarcinoma (COAD) tissues (n=456) and normal colon tissues (n=41) from the TCGA database. Data were presented as median with interquartile range (IQR). (f) Dot plots depicting the correlations between the expression of TAF1 and that of GPX4, FSP1, FTH1, and FTL in the TCGA COAD dataset. (g) Dot plots depicting the correlations between

Unedited

the expression of TAF1 and that of GPX4, FSP1, FTH1, and FTL in TCGA OV dataset. (h) Kaplan-Meier survival analyses of patients in the TCGA COAD dataset. (i) Kaplan-Meier survival analyses of patients in the TCGA OV dataset. $^{*}P < 0.05$; $^{**}P < 0.01$; $^{***}P < 0.001$; not statistically significant (ns), $P > 0.05$; two independent-sample Student's t tests (d and e). Figure (a) and (c) were generated using R software (v.4.2.2) package "VennDiagram" (v.1.7.3) through Hiplot Pro (https://hiplot.com.cn/), a comprehensive web service for biomedical data analysis and visualization.

In order to identify genes that may specifically regulate ferroptosis, we utilized a pro-apoptotic gene set, including BCL2 associated X (BAX), BCL2 antagonist/killer 1 (BAK1), cytochrome c, somatic (CYCS), apoptotic peptidase activating factor 1 (APAF1), caspase 3 (CASP3), and caspase 7 (CASP7), and a pro-necroptotic gene set, including receptor interacting serine/threonine kinase 1 (RIPK1), receptor interacting serine/threonine kinase 3 (RIPK3), and mixed lineage kinase domain like pseudokinase (MLKL), (Newton et al., 2024) to calculate pro-apoptosis and pro-necroptosis scores for each sample in the GDC Pan-Cancer dataset via gene set variation analysis (GSVA). Next, to identify those showing no association with apoptosis or necroptosis, we assessed the correlation between each score and the expression levels of the 177 genes (Fig. 1b). Considering that a Spearman's correlation coefficient $|\rho| < 0.2$ indicates poor or negligible correlation (Akoglu, 2018; Schober et al., 2018), we identified 90 genes exhibiting no significant association with either necroptosis or apoptosis (Fig. 1c).

Among these 90 genes, we further screened 27 genes whose expression levels were upregulated in colon adenocarcinoma (COAD) using GEPIA3 (https://gepia3.bioinfoliu.com/) (Kang et al., 2025). We subsequently examined the expression of these 27 genes in ovarian carcinoma patients using the GSE66957 dataset and identified 14 genes upregulated in primary ovarian carcinoma (Fig. 1d). Among these, TAF1 was consistently upregulated in both COAD and OV (Fig. 1e) and was thus selected for further investigation.

We next examined the relationship between TAF1 and ferroptosis suppressors in the TCGA COAD and OV datasets. In COAD, TAF1 mRNA expression was significantly and negatively correlated with all four canonical ferroptosis suppressors (GPX4, FSP1, FTL, and FTH1) (Fig. 1f). In OV, TAF1 was negatively correlated with GPX4, FTL and FTH1, but not with FSP1 (Fig. 1g). Notably, the strongest inverse correlation across both cancer types consistently occurred between TAF1 and GPX4, suggesting that TAF1 may act as a negative regulator of GPX4. Moreover, high TAF1 expression was associated with poor prognosis in both COAD (Fig. 1h) and OV (Fig. 1i). Collectively, these findings indicate that TAF1 may function as a potential driver of ferroptosis, particularly in COAD and OV.

3.2 Distinct regulatory roles of TAF1 in ferroptosis

In order to determine whether TAF1 regulates ferroptosis, we first examined its protein expression in normal, COAD and OV cell lines by western blotting. As shown in Fig. 2a, TAF1 protein levels were markedly elevated in RKO (CRC), SW620 (CRC), SKOV3 (OV), and A2780 (OV) cells compared with the normal human colon epithelial cell line NCM460. Using CRISPR/Cas9 technology, we established TAF1-knockout (TAF1-KO) cell lines (Figs. 2b-2e). These cells were subsequently treated with the GPX4 inhibitor 1S,3R-RSL3 (RSL3) to assess their sensitivity to ferroptosis. Interestingly, the effects of TAF1 loss varied among the cell lines. In SKOV3 and SW620 cells, TAF1 deficiency slightly increased resistance to RSL3 (Figs. 2f and S1a), whereas in RKO and A2780 cells, TAF1-KO markedly enhanced susceptibility to RSL3-induced ferroptosis (Figs. 2g and S1b).

Unedited

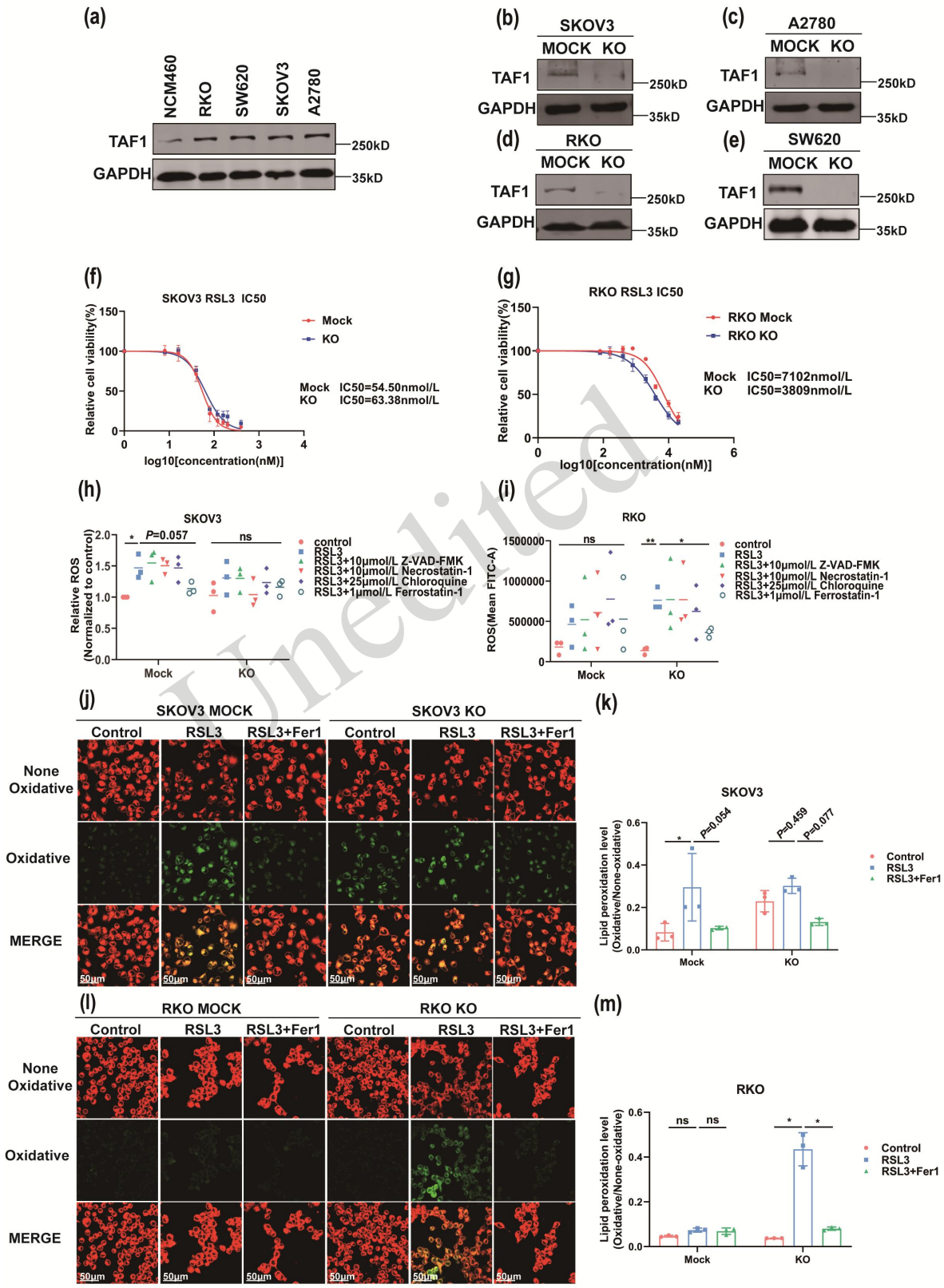

Unedited

Figure 2

Fig. 2 Distinct regulatory roles of TAF1 in ferroptosis

(a) Western blot analysis of TAF1 protein levels in NCM460, RKO, SW620, SKOV3, and A2780 cells. (b) Validation of TAF1 knockout in SKOV3 cells via western blotting. (c) Validation of TAF1 knockout in A2780 cells via western blotting. (d) Validation of TAF1 knockout in RKO cells via western blotting. (e) Validation of TAF1 knockout in SW620 cells via Western blotting. (f) Cell viability of TAF1-Mock and TAF1-KO cells treated with RSL3 for 48 h at the indicated concentrations in SKOV3 cells. (g) Cell viability of TAF1-Mock and TAF1-KO cells treated with RSL3 for 48 h at the indicated concentrations in RKO cells. (h) Intracellular ROS levels in SKOV3 TAF1-Mock and TAF1-KO cells treated with 100 nmol/L RSL3 in the absence or presence of Z-VAD-FMK, necrostatin-1, chloroquine or ferrostatin-1 for 24 h. (i) Intracellular ROS levels in RKO TAF1-Mock and TAF1-KO cells treated with 6 μmol/L RSL3 in the absence or presence of Z-VAD-FMK, necrostatin-1, chloroquine, or ferrostatin-1 for 48 h. (j, k) Representative images and quantitative analysis of lipid peroxidation (LPO) in SKOV3 TAF1-Mock and TAF1-KO cells treated with 100 nmol/L RSL3 for 24 h with or without ferrostatin-1. (l, m) Representative images and quantitative analysis of LPO in RKO TAF1-Mock and TAF1-KO cells treated with 6 μmol/L RSL3 for 48 h with or without ferrostatin-1. All experiments were performed in triplicate. Data are presented as mean ± SD (f, g, k and m) or mean (h and i). $^{*}P < 0.05$; $^{**}P < 0.01$; $^{***}P < 0.001$; not statistically significant (ns), $P > 0.05$; paired Student's t tests (h and i), one-way ANOVA (k and m).

Since the abnormal accumulation of ROS is a hallmark of ferroptosis, we next evaluated the ROS levels in TAF1-KO and Mock control cells under various conditions. In SKOV3 and SW620 Mock cells, RSL3 treatment significantly increased the ROS levels, which were reversed by ferrostatin-1 (a ferroptosis inhibitor) but not by Z-VAD-FMK (an apoptosis inhibitor), necrostatin-1 (a necroptosis inhibitor), or chloroquine (an autophagy inhibitor). However, RSL3 failed to induce ROS accumulation in SKOV3 TAF1-KO cells. In SW620 TAF1-KO cells, elevated ROS levels were not suppressed by ferrostatin-1 (Figs. 2h and S1c).

In contrast, in RKO and A2780 TAF1-KO cells, RSL3 treatment significantly increased ROS levels, which were abrogated by ferrostatin-1 but not by Z-VAD-FMK, necrostatin-1, or chloroquine. Notably, RSL3 did not induce ROS accumulation in RKO or A2780 Mock cells (Figs. 2i and S1d).

We further assessed the LPO levels in tumor cells. BODIPY staining revealed that RSL3 treatment markedly increased LPO in SKOV3 and SW620 TAF1-mock cells, an effect that was completely rescued by ferrostatin-1 (Figs. 2j, 2k, S1e and S1f). In contrast, RSL3 induced LPO accumulation only in RKO and A2780 TAF1-KO cells (Figs. 2l, 2m, S1g and S1h).

Collectively, these results demonstrate that TAF1 exerts opposing effects on ferroptosis regulation depending on the cellular context, acting as either a suppressor or promoter of ferroptotic signaling.

3.3 Contrasting effects of TAF1 on ferroptosis depending on p53 status

In order to elucidate how TAF1 exerts opposing effects on ferroptosis, we examined the expression of the SLC7A11-GPX4 axis, the ferritinophagy pathway, and other key ferroptosis regulators, including p53, acyl-CoA synthetase long chain family member 4 (ACSL4) and FSP1, in TAF1-Mock and TAF1-KO cells. Notably, the protein levels of p53 were markedly elevated in RKO and A2780 TAF1-KO cells (Figs. 3a and 3b) but remained unchanged in SW620 TAF1-KO cells (Fig. 3c). According to data from the Cancer Dependency Map (DepMap), RKO and A2780 cells express wild-type p53, whereas SW620 cells harbor p53 mutations (P309S and R273H) and SKOV3 cells are p53-null (Fig. 3d). Previous studies have demonstrated that TAF1 phosphorylates wild-type p53, promoting MDM2-mediated p53 degradation (Li et al., 2004; Yang et al., 2019). These findings suggest that the contrasting effects of TAF1 on ferroptosis may depend on the p53 status.

Unedited

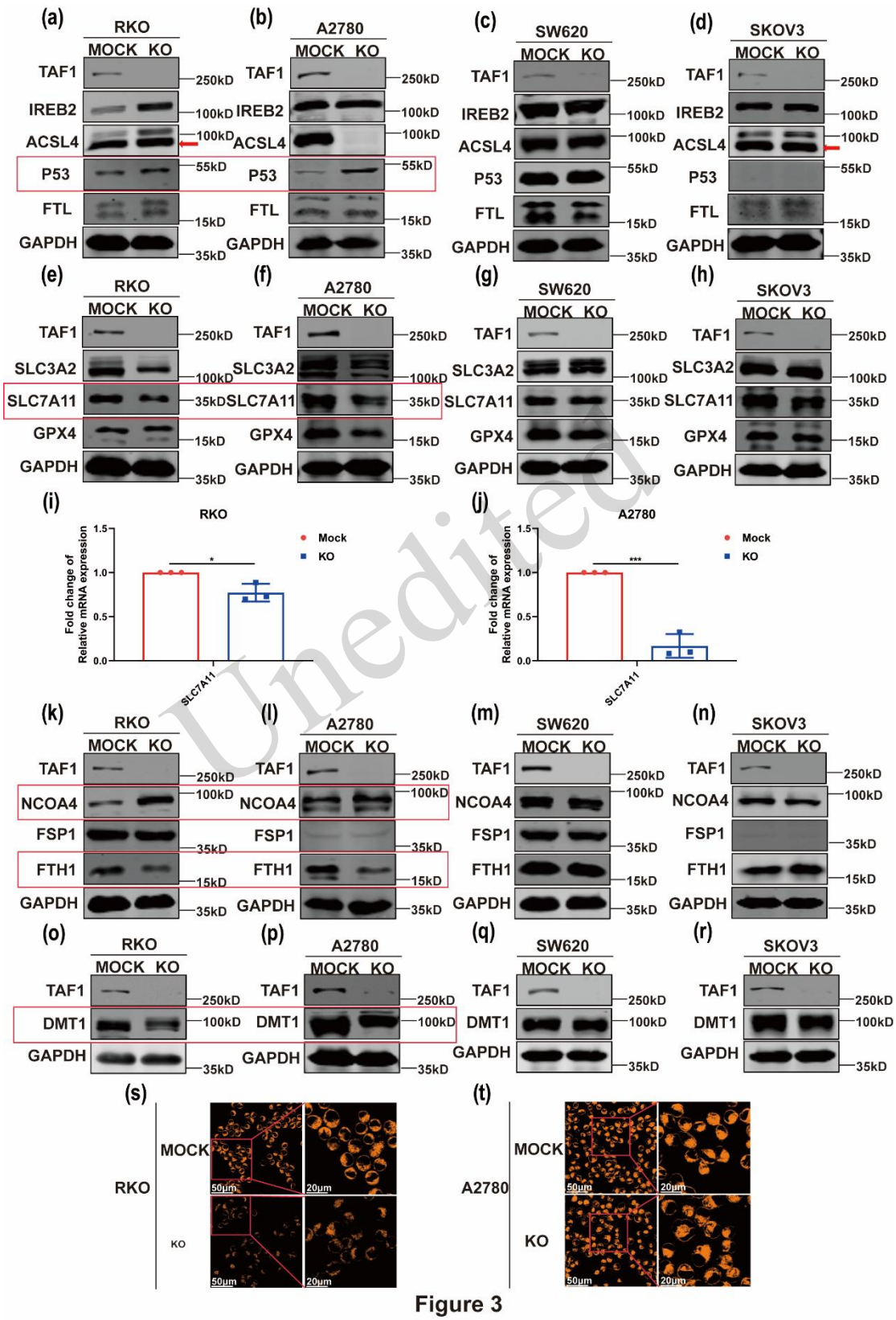

Unedited

Fig. 3 Contrasting effects of TAF1 on ferroptosis depending on p53 status

(a) Western blot analysis of iron responsive element binding protein 2 (IREB2), ACSL4, P53, and FTL protein levels in RKO

TAF1-Mock and TAF1-KO cells. The red arrow indicated the expected position of the ACSL4 band. The red box highlighted the protein with the most pronounced change. (b) Western blot analysis of IREB2, ACSL4, P53, and FTL protein levels in A2780 TAF1-Mock and TAF1-KO cells. The red box highlighted the protein with the most pronounced change. (c) Western blot analysis of IREB2, ACSL4, P53, and FTL protein levels in SW620 TAF1-Mock and TAF1-KO cells. (d) Western blot analysis of IREB2, ACSL4, P53, and FTL protein levels in SKOV3 TAF1-Mock and TAF1-KO cells. The red arrow indicated the expected position of the ACSL4 band. (e) Western blot analysis of SLC7A11-GPX4 axis in RKO TAF1-Mock and TAF1-KO cells. The red box highlighted the protein with the most pronounced change. (f) Western blot analysis of SLC7A11-GPX4 axis in A2780 TAF1-Mock and TAF1-KO cells. The red box highlighted the protein with the most pronounced change. (g) Western blot analysis of SLC7A11-GPX4 axis in SW620 TAF1-Mock and TAF1-KO cells. (h) Western blot analysis of SLC7A11-GPX4 axis in SKOV3 TAF1-Mock and TAF1-KO cells. (i) Relative mRNA expression levels of SLC7A11 in RKO TAF1-Mock and TAF1-KO cells. (j) Relative mRNA expression levels of SLC7A11 in A2780 TAF1-Mock and TAF1-KO cells. (k) Western blot analysis of NCOA4, FSP1 and FTH1 protein levels in RKO TAF1-Mock and TAF1-KO cells. The red box highlighted the protein with the most pronounced change. (l) Western blot analysis of NCOA4, FSP1 and FTH1 protein levels in A2780 TAF1-Mock and TAF1-KO cells. The red box highlighted the protein with the most pronounced change. (m) Western blot analysis of NCOA4, FSP1 and FTH1 protein levels in SW620 TAF1-Mock and TAF1-KO cells. (n) Western blot analysis of NCOA4, FSP1 and FTH1 protein levels in SKOV3 TAF1-Mock and TAF1-KO cells. (o) Western blot analysis of DMT1 protein levels in RKO TAF1-Mock and TAF1-KO cells. The red box highlighted the protein with the most pronounced change. (p) Western blot analysis of DMT1 protein levels in A2780 TAF1-Mock and TAF1-KO cells. The red box highlighted the protein with the most pronounced change. (q) Western blot analysis of DMT1 protein levels in SW620 TAF1-Mock and TAF1-KO cells. (r) Western blot analysis of DMT1 protein levels in SKOV3 TAF1-Mock and TAF1-KO cells. (s) Cellular Fe^{2+} detection in RKO TAF1-Mock and TAF1-KO cells using immunofluorescence assays. (t) Cellular Fe^{2+} detection in A2780 TAF1-Mock and TAF1-KO cells using immunofluorescence assays. All experiments were performed in triplicate. Data are presented as mean ± SD (i and j). $^{*}P < 0.05$; $^{**}P < 0.01$; $^{***}P < 0.001$; ns, $P > 0.05$; two independent-sample Student's t tests (i and j).

Unedited

We next analyzed SLC7A11, a canonical ferroptosis suppressor within the SLC7A11-GPX4 axis and a downstream target of p53 (Jiang et al., 2015). The knockout of TAF1 in p53 wild-type cells (RKO and A2780) significantly downregulated SLC7A11 protein expression (Figs. 3e and 3f), whereas no such change was observed in p53-mutant or p53-null cells (SW620 or SKOV3) (Figs. 3g and 3h). Consistent with the protein data, SLC7A11 mRNA levels were also decreased in p53 wild-type TAF1-KO cells, in agreement with previous reports (Jiang, et al., 2015) (Figs. 3i and 3j).

In addition to SLC7A11, we found that TAF1 knockout upregulated nuclear receptor coactivator 4 (NCOA4), a selective cargo receptor mediating ferritinophagy, thereby promoting ferritin degradation (Hou, et al., 2016) in RKO and A2780 cells (Figs. 3k and 3l). However, no changes in NCOA4 expression were detected in p53-mutant cells (Figs. 3m and 3n). Interestingly, TAF1 knockout decreased the protein levels of FTH1 and divalent metal transporter 1 (DMT1) in both RKO and A2780 cells (Figs. 3k, 3l, 3o and 3p), whereas no alteration was detected in SW620 or SKOV3 cells (Figs. 3m, 3n, 3q and 3r), suggesting that TAF1 may also influence intracellular iron homeostasis in p53 wild-type cells.

We next measured the levels of labile ferrous iron in TAF1-Mock and TAF1-KO cells. The deletion of TAF1 significantly reduced the labile iron pool in RKO cells (Fig. 3s) but did not alter the iron levels in A2780, SW620, or SKOV3 cells (Figs. 3t, S2a and S2b). This discrepancy between labile iron levels and ferroptosis sensitivity in RKO and A2780 cells indicates that additional yet unidentified mechanisms may contribute to the cell-type-specific regulation of ferroptosis by TAF1.

Collectively, these findings demonstrate that TAF1 facilitates MDM2-mediated degradation of wild-type p53, thereby upregulating SLC7A11 expression and enhancing resistance to ferroptosis. These results highlight the pivotal role of p53 status in determining the dual regulatory effects of TAF1 on ferroptosis.

3.4 TAF1-mediated regulation of ferroptosis in p53-mutant cells via ubiquitin-proteasome-mediated degradation of nGPX4

In order to further elucidate how TAF1 regulates ferroptosis in p53-mutant cells, we explored its potential transcriptional and post-transcriptional roles. Given that TAF1 is the largest subunit of the TFIID complex, we initially hypothesized that TAF1 might influence ferroptosis through transcriptional regulation. To test this notion, we performed RNA sequencing (RNA-seq) analysis, which revealed no significant differences in the

global transcriptome profiles following RSL3 or RSL3 + ferrostatin-1 treatment in both SKOV3 Mock and TAF1-KO cells (Fig. 4a). Differential expression and pathway enrichment analyses identified no ferroptosis-related genes or pathways in either the GO or KEGG databases (Figs. S3a–S3d).

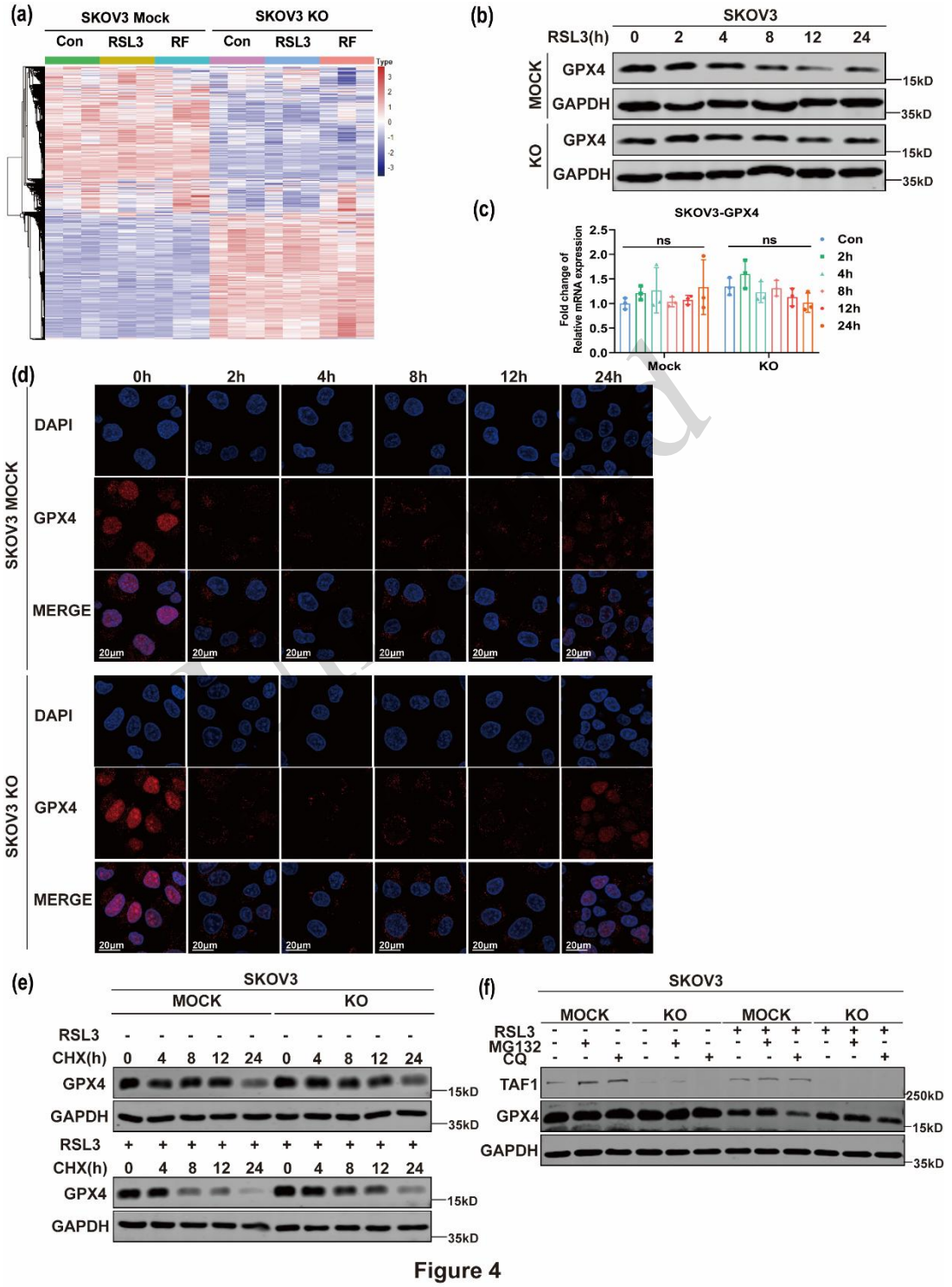

Figure 4

Fig. 4 TAF1-mediated regulation of ferroptosis in p53-mutant cells via ubiquitin-proteasome-mediated degradation of nGPX4

(a) Heatmap showing differentially expressed genes in SKOV3 TAF1-Mock and TAF1-KO cells treated with the indicated agents. (b) Western blot analysis of GPX4 protein levels in SKOV3 TAF1-Mock and TAF1-KO cells treated with 100 nmol/L

RSL3 for the indicated times. (c) Fold changes in the relative GPX4 mRNA levels in SKOV3 TAF1-Mock and TAF1-KO cells treated with 100 nmol/L RSL3 for the indicated times. (d) Immunofluorescence staining of GPX4 in SKOV3 TAF1-Mock and TAF1-KO cells treated with 100 nmol/L RSL3 for the indicated times. (e) Western blot analysis of GPX4 protein stability in SKOV3 TAF1-Mock and TAF1-KO cells treated with 100 nmol/L RSL3 for 4 h, followed by incubation with 50 μg/mL cycloheximide (CHX) for the indicated durations. (f) Western blot analysis of GPX4 protein levels in SKOV3 TAF1-Mock and TAF1-KO cells treated with 100 nmol/L RSL3 for 24 h, followed by co-treatment with 10 μmol/L MG132 or 25 μmol/L chloroquine (CQ) for 4 h. All experiments were performed in triplicate. Data are presented as mean ± SD (c). $^{*}P < 0.05$; $^{**}P < 0.01$; $^{***}P < 0.001$; ns, $P > 0.05$; one-way ANOVA (c).

Interestingly, TAF1 knockout prevented the RSL3-induced reduction of GPX4 protein levels (Fig. 4b), while the GPX4 mRNA levels remained unchanged (Fig. 4c). A similar pattern was observed in SW620 cells, where TAF1 deletion stabilized GPX4 protein expression (Figs. S4a and S4b), suggesting that TAF1 may regulate the degradation rather than the transcription of GPX4 protein. Confocal microscopy further confirmed that TAF1 promoted the degradation of nGPX4 (Figs. 4d and S4c). Consistently, the CHX chase assays demonstrated that TAF1 accelerated GPX4 degradation (Figs. 4e and S4d) and reduced its protein half-life (Figs. S4e and S4f).

Since GPX4 degradation can occur through either the ubiquitin-proteasome pathway (Sun et al., 2023; Wang et al., 2023) or autophagy (Wu et al., 2019; Xue et al., 2023), we next sought to determine which mechanism was involved in TAF1-mediated GPX4 turnover. Co-treatment of SKOV3 and SW620 cells with RSL3 and either the proteasome inhibitor MG132 or the autophagy inhibitor chloroquine (CQ) revealed that only MG132 restored the GPX4 protein levels (Figs. 4f and S4g).

Collectively, these findings indicate that TAF1 promotes the degradation of nuclear GPX4 via the ubiquitin-proteasome system in p53-mutant cells, thereby modulating ferroptosis independently of transcriptional regulation.

Unedited

3.5 TAF1-mediated K11-linked ubiquitination of nGPX4

In order to determine whether TAF1 interacts with and promotes nGPX4 ubiquitination, we co-transfected FLAG-tagged TAF1 and HA-tagged nGPX4 into HEK293T cells. Immunoprecipitation assays confirmed that HA-nGPX4 was pulled down by FLAG-TAF1 (Fig. 5a). Conversely, FLAG-nGPX4 co-precipitated GFP-TAF1 (Fig. S5a), further validating their interaction. Domain architecture analysis revealed that TAF1 contains N-terminal and C-terminal kinase domains (Dikstein, et al., 1996), a histone acetyltransferase (HAT) domain (Mizzen, et al., 1996), and a ubiquitin-activating/conjugating (E1/E2) domain (Pham, 2000). Based on Pfam annotations (Mistry et al., 2021), we constructed four FLAG-tagged truncated TAF1 variants, each containing one of the following domains: the N-terminal kinase domain (FLAG-TBP), the HAT domain (FLAG-DUF), the E1/E2 domain (FLAG-ZINC), and the C-terminal kinase domain (FLAG-BRD) (Fig. 5b). Immunoprecipitation assays showed that FLAG-DUF, but not FLAG-ZINC, interacted with HA-nGPX4 (Figs. 5c and S5b).

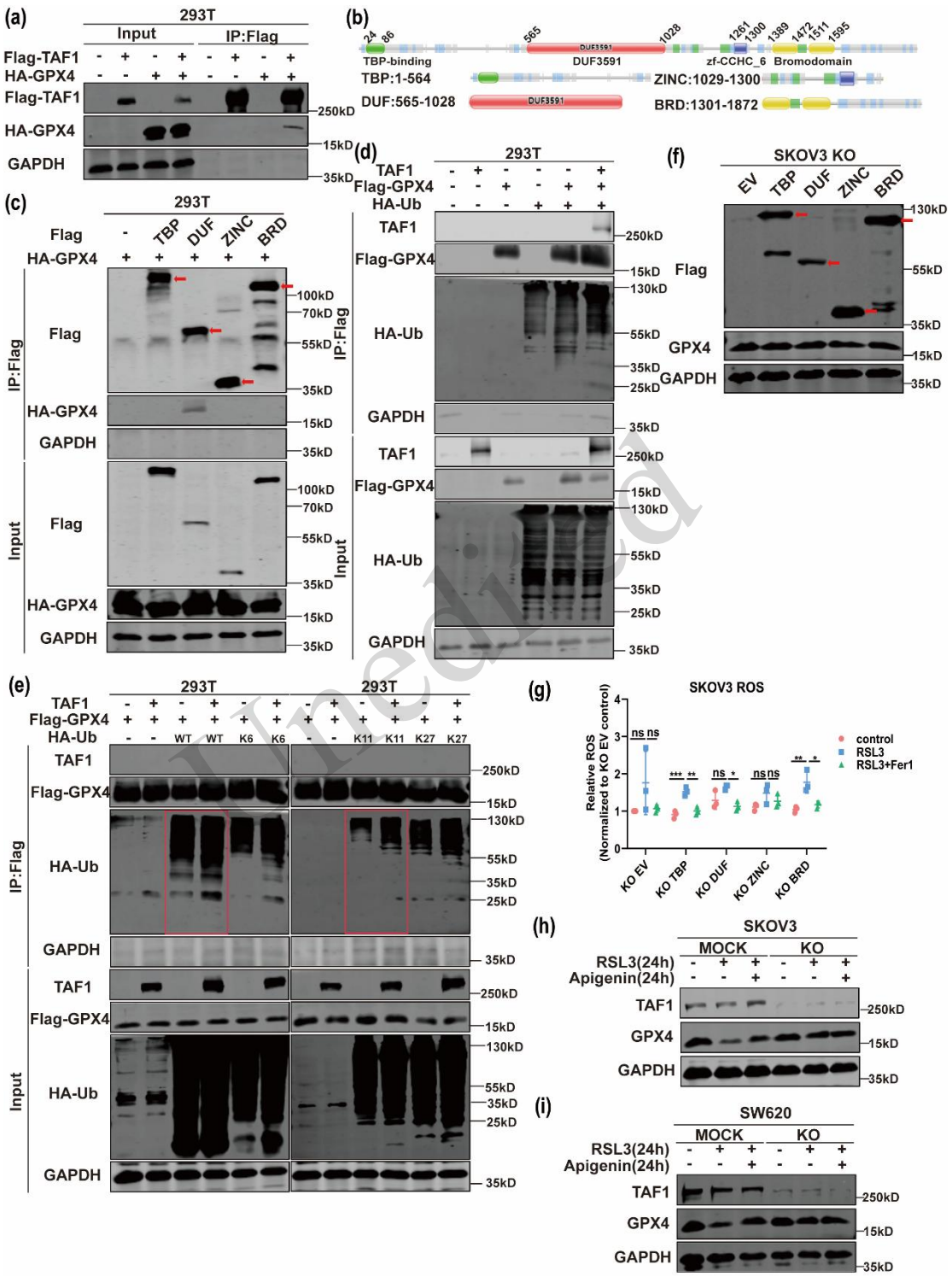

Figure 5

Fig. 5 TAF1-mediated K11-linked ubiquitination of nGPX4

(a) Western blot analysis showing the co-immunoprecipitation of exogenous FLAG-tagged TAF1 and HA-tagged nGPX4 in HEK293T cells. (b) Schematic representation of truncated TAF1 constructs. (c) Western blot analysis showing the co-immunoprecipitation of exogenous FLAG-tagged TAF1 truncations, designed based on the domain architecture shown in (b), with HA-tagged nGPX4 in HEK293T cells. (d) Ubiquitination assay of FLAG-tagged nGPX4 in the presence of GFP-tagged TAF1. (e) HEK293T cells were co-transfected with GFP-TAF1 and FLAG-nGPX4 together with either wild-type

(WT) ubiquitin or the indicated ubiquitin mutants. After treatment with MG132 (10 μmol/L) for 4 h, cells were harvested for immunoprecipitation and western blot analysis. The red box highlighted the protein with the most pronounced change. (f) Western blot analysis of exogenous FLAG-tagged truncated TAF1 proteins expressed in SKOV3 TAF1-KO cells. (g) Intracellular ROS levels in SKOV3 TAF1-KO cells transfected with different FLAG-tagged TAF1 truncations and treated with the indicated agents for 24 h. (h) Western blot analysis of GPX4 in SKOV3 TAF1-Mock and TAF1-KO cells treated with 100 nmol/L RSL3 and 10 μmol/L apigenin for 24 h. (i) Western blot analysis of GPX4 in SW620 TAF1-Mock and TAF1-KO cells treated with 2.5 μmol/L RSL3 and 20 μmol/L apigenin for 24 h. All experiments were performed in triplicate. Data are presented as mean ± SD (g). $^{*}P < 0.05$; $^{**}P < 0.01$; $^{***}P < 0.001$; ns, $P > 0.05$; one-way ANOVA (g).

Notably, the overexpression of full-length TAF1 markedly increased the ubiquitination of nGPX4 (Fig. 5d). As polyubiquitin chains can be linked through seven distinct lysine residues (K6, K11, K27, K29, K33, K48, and K63) of ubiquitin (Mevissen and Komander, 2017), we generated seven HA-tagged ubiquitin mutants, each containing only a single lysine residue. Co-transfection of these mutants with FLAG-nGPX4 and GFP-TAF1 in HEK293T cells revealed that TAF1 overexpression specifically enhanced the K11-linked polyubiquitination of nGPX4 (Fig. 5e and S5c). Collectively, these findings demonstrate that TAF1 mediates the K11-linked ubiquitination of nGPX4, thereby facilitating its degradation.

In order to assess whether the DUF domain of TAF1 contributes to ferroptosis regulation, we overexpressed the four FLAG-tagged truncated TAF1 variants in SKOV3 TAF1-KO cells (Fig. 5f). Following treatment with RSL3 or RSL3 combined with ferrostatin-1, intracellular ROS levels were measured. Remarkably, only the overexpression of FLAG-TBP and FLAG-BRD, which harbor the N- and C-terminal kinase domains, respectively, increased the sensitivity of SKOV3 TAF1-KO cells to RSL3-induced ferroptosis (Fig. 5g). These results suggest that the kinase domains of TAF1 play a crucial role in ferroptosis regulation.

In order to further explore the role of TAF1 kinase activity, SKOV3 Mock and KO cells were treated with RSL3 in the presence or absence of apigenin, a known inhibitor of TAF1 kinase activity (Li, et al., 2004). Western blot analysis showed that apigenin effectively prevented GPX4 degradation induced by RSL3 treatment (Figs. 5h and 5i). Together, these findings demonstrate that TAF1 promotes GPX4 degradation via its kinase domain, thereby regulating ferroptosis in p53-mutant cells.

Unedited

3.6 TAF1-mediated enhancement of ferroptosis in p53-mutant xenografts

Given that TAF1 promotes ferroptosis in p53-mutant cells in vitro, we next investigated its role in vivo. For this purpose, subcutaneous xenograft tumors were established in nude mice using SW620 TAF1-Mock and TAF1-KO cells (Fig. 6a). Treatment with RSL3 markedly suppressed tumor growth in the TAF1-Mock group, whereas no significant inhibition was observed in the TAF1-KO group (Figs. 6b and 6c). Although RSL3 treatment tended to reduce tumor weight in the TAF1-Mock group, no such trend was evident in the TAF1-KO group (Fig. 6d). While these differences were not statistically significant, the data suggest that TAF1 knockout confers resistance to RSL3-induced tumor suppression. Furthermore, immunohistochemical analysis revealed reduced GPX4 expression and increased 4-hydroxynonenal (4-HNE) accumulation in TAF1-Mock tumors following RSL3 treatment, whereas GPX4 and 4-HNE levels remained largely unchanged in TAF1-KO tumors (Fig. 6e). Collectively, these findings indicate that TAF1 enhances ferroptosis in vivo in p53-mutant xenograft models.

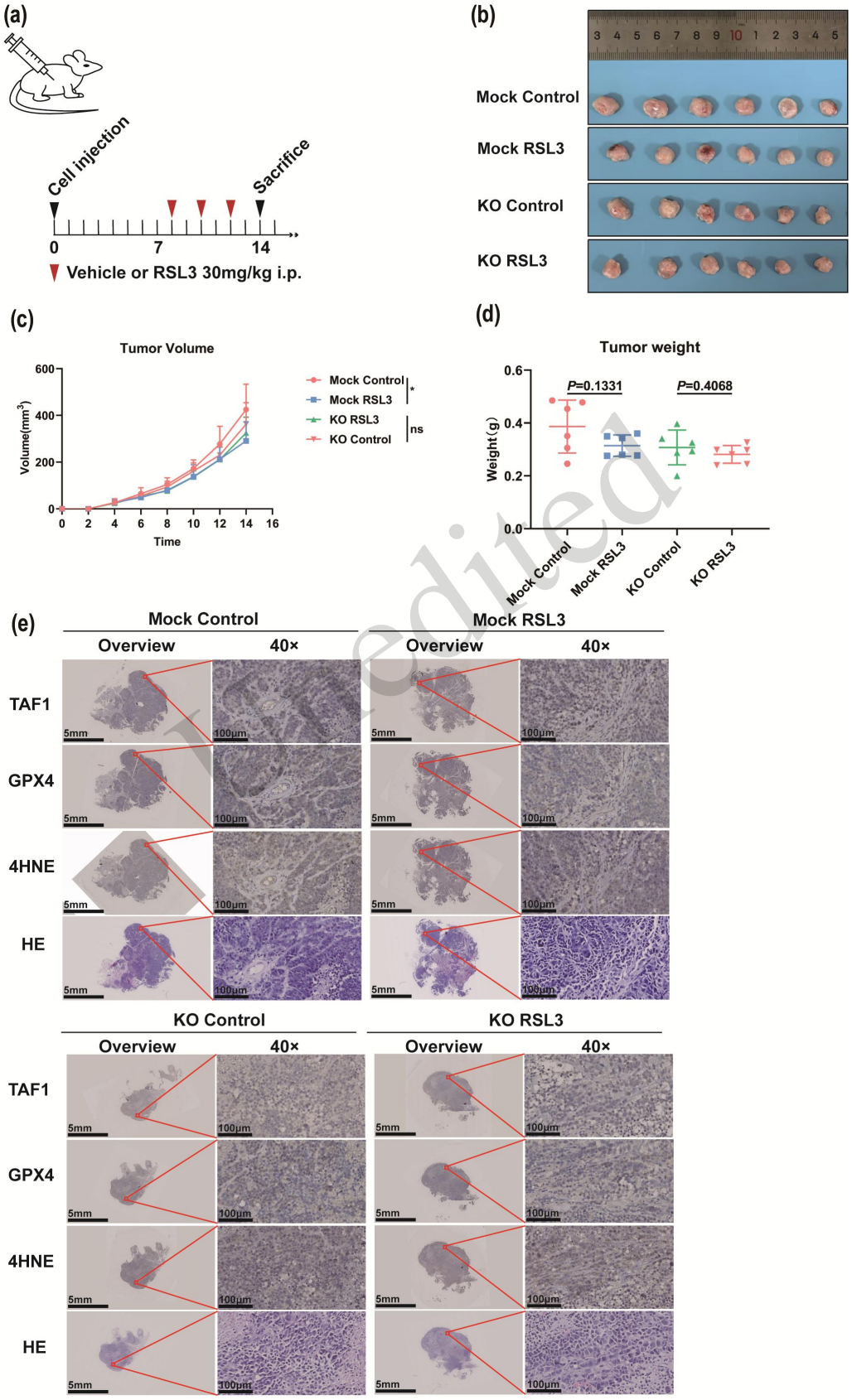

Figure 6

Unedited

Fig. 6 TAF1-mediated enhancement of ferroptosis in p53-mutant xenografts

(a) Schematic illustration of the experimental design showing the establishment of subcutaneous xenograft tumors in nude mice and the treatment regimen. (b) Representative images of tumors derived from SW620 TAF1-Mock and TAF1-KO cells in mice treated with or without RSL3 (n = 6). (c) Tumor growth curves showing the xenograft volumes measured over time (n = 6). (d) Final tumor weights measured at the experimental endpoint (n = 6). (e) Representative immunohistochemical staining of TAF1, GPX4, and 4-HNE, as well as H&E staining of TAF1-Mock and TAF1-KO xenograft tumors.

4 Discussion

Ferroptosis, a distinct form of regulated cell death characterized by plasma membrane rupture due to the aberrant accumulation of iron-dependent phospholipid hydroperoxides (Yan et al., 2021), has been implicated in tumor suppression and increased sensitivity to chemotherapy (Roh et al., 2016; Sun et al., 2016; Roh et al., 2017; Sato et al., 2018). Despite its clinical significance, the molecular mechanisms governing ferroptosis remain incompletely understood. In this study, we identified TAF1 as a critical regulator of ferroptosis that exerts dual functions depending on the p53 status of cells. In p53-mutant cells, TAF1 promotes the K11-linked ubiquitination and subsequent degradation of nGPX4, thereby facilitating ferroptosis. Conversely, in p53 wild-type cells, TAF1 enhances MDM2-mediated p53 degradation, resulting in SLC7A11 upregulation and resistance to ferroptosis (Fig. 7).

Unedited

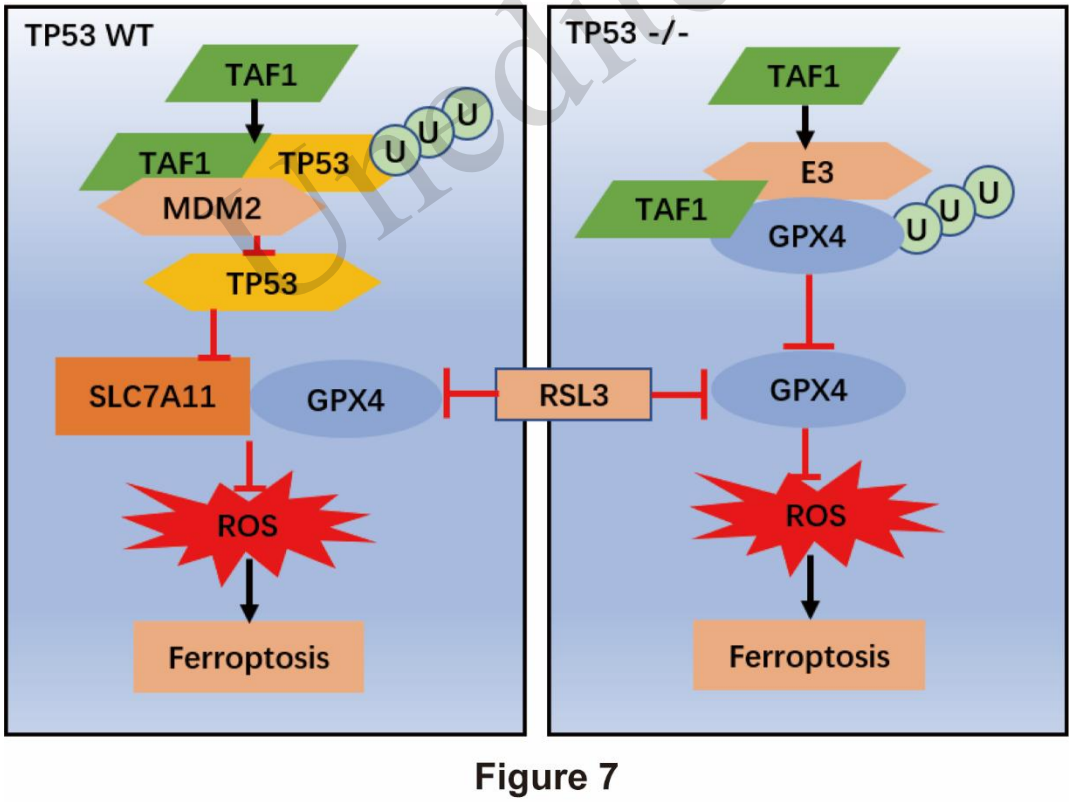

Fig. 7 Schematic illustration of TAF1-mediated ferroptosis regulation.

TAF1 promotes ferroptosis in p53-mutant cells by facilitating the K11-linked ubiquitination and subsequent degradation of nGPX4. In p53 wild-type cells, TAF1 enhances the MDM2-mediated degradation of p53, leading to the upregulation of SLC7A11 expression and conferring resistance to ferroptosis.

TAF1, the largest subunit of the transcription factor IID (TFIID) complex, participates in diverse cellular processes including phosphorylation, histone acetylation, ubiquitin activation, and ubiquitin conjugation.

Beyond its established role in neurodegenerative diseases, TAF1 has been implicated in tumorigenesis: it promotes colon cancer cell proliferation by facilitating G1-phase progression through p53 phosphorylation (Li, et al., 2004) and contributes to leukemogenesis by acetylating the fusion transcription factor AML1-ETO (Xu, et al., 2019). TAF1 enhances epithelial-mesenchymal transition (EMT) in non-small-cell lung cancer (NSCLC) (Zhang et al., 2022) and increases paclitaxel resistance in esophageal cancer (Zhang et al., 2023). Moreover, the inhibition of TAF1 induces apoptosis (Zhou, et al., 2021) and autophagy (Liu and Gu, 2022). However, the relationship between TAF1 and ferroptosis has remained unexplored. Our study reveals that TAF1 exhibits context-dependent functions in ferroptosis based on p53 status, highlighting its potential as a therapeutic target for ferroptosis-related interventions. Notably, several TAF1 inhibitors, such as BAY-299 (Zhou, et al., 2021; Dibra et al., 2024), N2817 (Su et al., 2023), and BI-2536 (Puglisi et al., 2012), have demonstrated potent anticancer activity, while whether these inhibitors also modulate ferroptosis warrants further investigation.

The p53 protein is known as a key regulator of ferroptosis, orchestrating both canonical and noncanonical pathways (Liu and Gu, 2022); however, its role in ferroptotic regulation is complex, especially in metabolic contexts. Wild-type p53 represses SLC7A11 expression, thereby promoting ferroptosis. An acetylation-defective mutant, $p53^{3KR}$, retains this ability (Jiang, et al., 2015), whereas other hotspot mutations impair ferroptotic sensitivity. For example, $p53^{R172H}$ and $p53^{R245W}$ suppress ferroptosis via the NRF2-dependent regulation of microsomal glutathione S-transferase 3 (MGST3) and peroxiredoxin 6 (PRDX6) (Dibra, et al., 2024), while $p53^{R175H}$ enhances tumor growth by binding to and inhibiting BACH1-mediated SLC7A11 downregulation (Su, et al., 2023). Our findings further indicate that the functional outcome of TAF1 depends on p53 status. In p53 wild-type cells, TAF1 facilitates the MDM2-mediated degradation of phosphorylated p53, leading to the upregulation of SLC7A11 and resistance to ferroptosis—consistent with previous observations (Jiang, et al., 2015). In contrast, in p53-null (SKOV3) and p53-mutant (SW620, harboring $p53^{R273H}$ and $p53^{P309S}$ mutations) cells, TAF1 phosphorylates and promotes the degradation of nuclear GPX4, thereby triggering ferroptosis. Given that TAF1 phosphorylates both p53 and GPX4, and that p53 can directly interact with GPX4 (Qian, et al., 2023), we propose that p53 and nGPX4 may compete for TAF1 binding. The precise molecular mechanisms underlying this competition, however, require further elucidation.

GPX4 exists in three major isoforms localized in the cytosol (cGPX4), mitochondria (mGPX4), and nucleus (nGPX4), respectively. (Xie, et al., 2023). While cGPX4 and mGPX4 have been studied extensively, the physiological role of nGPX4 remains poorly understood. Initially identified in murine male germ cells, nGPX4 associates with the sperm nuclear matrix and facilitates chromatin decondensation during fertilization (Puglisi, et al., 2012). More recently, nGPX4—also referred to as inducible GPX4 (iGPX4)—was reported to promote ferroptosis in metabolic-associated fatty liver disease (MAFLD) by driving cGPX4 oligomerization into enzymatically inactive complexes (Tong et al., 2022). In contrast, our study uncovers a previously unrecognized protective role of nGPX4, namely that it acts as a nuclear antioxidant defense against phospholipid hydroperoxide-induced ferroptosis. This finding challenges the prevailing view of nGPX4 as being a pro-ferroptotic factor and suggests that nuclear GPX4 may exert context-dependent regulatory functions in ferroptosis.

Previous research has identified several mechanisms governing GPX4 degradation. Members of the tripartite motif (TRIM) protein family, including TRIM25 (Li et al., 2023) and TRIM26 (Wang, et al., 2023), catalyze GPX4 ubiquitination and degradation. Additionally, chaperone-mediated autophagy contributes to GPX4 turnover (Wu, et al., 2019). However, these studies primarily focus on cGPX4 and mGPX4, leaving the regulatory mechanisms of nGPX4 largely unexplored. Herein, we demonstrated that TAF1 directly mediates nGPX4 degradation in p53-mutant cells by promoting its K11-linked polyubiquitination and subsequent proteasomal degradation, representing a novel pathway by which TAF1 regulates ferroptosis in the context of p53 mutation.

Despite these promising findings, several key questions remain. First, we observed that TAF1-mediated nGPX4 degradation occurred only upon RSL3 treatment. RSL3 has been regarded as a selective GPX4 inhibitor that covalently binds to the enzyme's active site, thereby suppressing its catalytic activity (Yang, et al., 2014;

Unedited

Yang, et al., 2016). However, a recent report suggested that RSL3 does not directly inhibit GPX4 activity but rather alters its electrophoretic migration in gels (Cheff et al., 2023). This observation implies that RSL3 may chemically modify GPX4, and we speculate that such modification enhances the interaction between TAF1 and GPX4. Nevertheless, the exact mechanism remains unclear, and further biochemical and structural investigations are required to elucidate the underlying processes. Moreover, although TAF1 promotes nGPX4 ubiquitination and degradation, the specific ubiquitin-activating enzyme (E1), conjugating enzyme (E2), and ligase (E3) involved have not yet been identified. Given that TAF1 contains intrinsic kinase and ubiquitin-related domains, it is plausible that TAF1 itself may function as an E1 or E2 enzyme within this pathway. Therefore, identifying the E3 ligase responsible for nGPX4 ubiquitination will be an important direction of future research.

5 Conclusions

This study provides critical insights into the molecular mechanisms regulating ferroptosis and establishes a foundation for precision medicine approaches. In p53 wild-type tumors, low TAF1 expression may serve as a predictive biomarker for the efficacy of ferroptosis-based therapies. Conversely, in p53-mutant tumors with high TAF1 expression, patients may benefit more from treatment with ferroptosis inducers. Collectively, our study highlights the potential of targeting TAF1 to develop genotype-specific ferroptosis-based therapeutic strategies, paving the way for more effective and personalized cancer treatment options.

Unedited

Data availability statement

Total RNA expression profiling data from 12 OV patients and 57 healthy donors were obtained from the GSE66957 dataset available in the GEO database(https://www.ncbi.nlm.nih.gov/geo/query/acc.cgi?acc=GSE66957). In addition, TCGA OV dataset and COAD dataset were retrieved from the UCSC Xena platform (https://xenabrowser.net/). The RNA-seq data of SKOV3 TAF1-Mock and TAF1- KO cell lines` following RSL3 or RSL3 + ferrostatin-1 treatment has been deposited into the Sequence Read Archive (SRA) database and can be accessed at https://dataview.ncbi.nlm.nih.gov/object/PRJNA1231572?reviewer=12p99qgq97obj0hc1s2anmq4i9. All other research data can be obtained from the authors upon reasonable request.

Acknowledgments

This work was supported by National Natural Science Foundation of China [grant number 82473008, 82173223 and 82303644], the CAMS Innovation Fund for Medical Sciences [grant number 2019-I2M-5-044] and Zhejiang Medical and Health Science and Technology Project [Grant No.2025KY439].

We thank Qiong HUANG from the Core Facilities, Zhejiang University School of Medicine for their technical support. We thank Shanghai Tengyun Biotechnology Co., Ltd. for developing Hiplot Pro platform (https://hiplot.com.cn/) and providing technical assistance and valuable tools for data analysis and visualization.

Author contributions

Kehong YE, Chaoyi CHEN, and Honghe ZHANG proposed the scientific question. Kehong YE, Chaoyi CHEN, and Liang SUN designed the experiments and conducted the research. Kehong YE, Xuan LAI, Yinjun HE, and Ming ZHU established the animal models. Kehong YE and Chaoyi CHEN performed the data analysis. Kehong YE drafted the manuscript, and Liang SUN and Xuan LAI assisted in manuscript revision. Honghe ZHANG, Chaoyi CHEN, and Meifu GAN provided funding support for the project. Honghe ZHANG and Weiqin JIANG conceived the overall study and coordinated the research team. All authors read and approved the final manuscript and, therefore, had full access to all the data in the study and take responsibility for the integrity and security of the data.

Compliance with ethics guidelines

Kehong YE, Meifu GAN, Liang SUN, Chaoyi CHEN, Xuan LAI, Yinjun HE, Ming ZHU, Weiqin JIANG and Honghe ZHANG declare that they have no conflict of interest.

All institutional and national guidelines for the care and use of laboratory animals were followed. All animal experiments were conducted in accordance with protocols approved by the Institutional Animal Care and Use Committee of Zhejiang

University (Ethics Committee number: ZJU20240161).

References

Akoglu H, 2018. User's guide to correlation coefficients. *Turkish Journal of Emergency Medicine*, 18(3):91–93 %U https://www.sciencedirect.com/science/article/pii/S2452247318302164.

Aneichyk T, Hendriks WT, Yadav R, et al., 2018. Dissecting the causal mechanism of x-linked dystonia-parkinsonism by integrating genome and transcriptome assembly. *Cell*, 172(5):897–909.e821 %U https://linkinghub.elsevier.com/retrieve/pii/S0092867418301557.

Bersuker K, Hendricks JM, Li Z, et al., 2019. The coq oxidoreductase fsp1 acts parallel to gpx4 to inhibit ferroptosis. *Nature*, 575(7784):688–692 %U http://www.nature.com/articles/s41586–41019–41705–41582.

Cheff DM, Huang C, Scholzen KC, et al., 2023. The ferroptosis inducing compounds rsl3 and ml162 are not direct inhibitors of gpx4 but of txnrd1. *Redox Biology*, 62:102703 %U https://www.sciencedirect.com/science/article/pii/S2213231723001040.

Chen X, Kang R, Kroemer G, et al., 2021. Broadening horizons: The role of ferroptosis in cancer %u http://www.Nature.Com/articles/s41571-020-00462-0. *Nature Reviews Clinical Oncology*,

Cheng H, Capponi S, Wakeling E, et al., 2020. Missense variants in taf1 and developmental phenotypes: Challenges of determining pathogenicity. *Human Mutation*, 41(2):449–464 %* © 2019 Wiley Periodicals, Inc. %U https://onlinelibrary.wiley.com/doi/abs/2010.1002/humu.23936.

Deng F, Zhao B-C, Yang X, et al., 2021. The gut microbiota metabolite capsiate promotes gpx4 expression by activating trpv1 to inhibit intestinal ischemia reperfusion-induced ferroptosis. *Gut Microbes*, 13(1):1902719 %U https://doi.org/1902710.1901080/19490976.19492021.11902719.

Dibra D, Xiong S, Moyer SM, et al., 2024. Mutant p53 protects triple-negative breast adenocarcinomas from ferroptosis in vivo. *Science Advances*, 10(7):eadk1835 %U https://www.science.org/doi/1810.1126/sciadv.adk1835.

Dikstein R, Ruppert S, Tjian R, 1996. Tafii250 is a bipartite protein kinase that phosphorylates the basal transcription factor rap74. *Cell*, 84(5):781–790 %U https://www.sciencedirect.com/science/article/pii/S0092867400810557.

Dixon SJ, Lemberg KM, Lamprecht MR, et al., 2012. Ferroptosis: An iron-dependent form of nonapoptotic cell death. *Cell*, 149(5):1060–1072.

Dixon SJ, Patel DN, Welsch M, et al., 2014. Pharmacological inhibition of cystine–glutamate exchange induces endoplasmic reticulum stress and ferroptosis. *eLife*, 3:e02523 %U https://doi.org/02510.07554/eLife.02523.

Dobin A, Davis CA, Schlesinger F, et al., 2013. Star: Ultrafast universal rna-seq aligner. *Bioinformatics*, 29(1):15–21 %U https://doi.org/10.1093/bioinformatics/bts1635.

Doll S, Freitas FP, Shah R, et al., 2019. Fsp1 is a glutathione-independent ferroptosis suppressor. *Nature*, 575(7784):693–698 %U http://www.nature.com/articles/s41586–41019–41707–41580.

Feng Z-W, Yang C-F, Xiao H-F, et al., 2024. Ythdc1 regulates the migration, invasion, proliferation, and apoptosis of rheumatoid fibroblast-like synoviocytes. *Frontiers in Immunology*, 15 %U https://www.frontiersin.org/journals/immunology/articles/10.3389/fimmu.2024.1440398/full

Goldman MJ, Craft B, Hastie M, et al., 2020. Visualizing and interpreting cancer genomics data via the xena platform. *Nature Biotechnology*, 38(6):675–678.

Guo Y-Y, Liang N-N, Zhang X-Y, et al., 2024. Mitochondrial gpx4 acetylation is involved in cadmium-induced renal cell ferroptosis. *Redox Biology*, 73:103179 %U https://www.sciencedirect.com/science/article/pii/S2213231724001575.

Hou W, Xie Y, Song X, et al., 2016. Autophagy promotes ferroptosis by degradation of ferritin. *Autophagy*, 12(8):1425–1428 %U https://doi.org/1410.1080/15548627.15542016.11187366.

Janakiraman U, Dhanalakshmi C, Yu J, et al., 2020. The investigation of the t-type calcium channel enhancer sak3 in an animal model of taf1 intellectual disability syndrome. *Neurobiology of Disease*, 143:105006 %U https://linkinghub.elsevier.com/retrieve/pii/S0969996120302813.

Jiang L, Kon N, Li T, et al., 2015. Ferroptosis as a p53-mediated activity during tumour suppression. *Nature*, 520(7545):57–62 %* 2015 Nature Publishing Group, a division of Macmillan Publishers Limited. All Rights Reserved. %U https://www.nature.com/articles/nature14344.

Kang Y-J, Pan L, Liu Y, et al., 2025. Gepia3: Enhanced drug sensitivity and interaction network analysis for cancer research. *Nucleic Acids Research*, 53(W1):W283–W290 %* https://creativecommons.org/licenses/by–nc/284.280/ %U https://academic.oup.com/nar/article/253/W281/W283/8139788.

Li B, Dewey CN, 2011. Rsem: Accurate transcript quantification from rna-seq data with or without a reference

Unedited

genome.
Li H-H, Li AG, Sheppard HM, et al., 2004. Phosphorylation on thr-55 by taf1 mediates degradation of p53: A role for taf1 in cell g1 progression. *Molecular Cell*, 13(6):867–878 %U https://www.sciencedirect.com/science/article/pii/S1097276504001236.
Li J, Liu J, Zhou Z, et al., 2023. Tumor-specific gpx4 degradation enhances ferroptosis-initiated antitumor immune response in mouse models of pancreatic cancer. *SCIENCE TRANSLATIONAL MEDICINE*,
Liu Y, Gu W, 2022. P53 in ferroptosis regulation: The new weapon for the old guardian. *Cell Death & Differentiation*, 29(5):895–910 %* 2022 The Author(s), under exclusive licence to ADMC Associazione Differenziamento e Morte Cellulare %U https://www.nature.com/articles/s41418–41022–00943–y.
Love MI, Huber W, Anders S, 2014. Moderated estimation of fold change and dispersion for rna-seq data with deseq2. *Genome Biology*, 15(12):550 %U https://genomebiology.biomedcentral.com/articles/510.1186/s13059–13014–10550–13058.
Mao C, Liu X, Zhang Y, et al., 2021. Dhodh-mediated ferroptosis defence is a targetable vulnerability in cancer %u http://www.Nature.Com/articles/s41586-021-03539-7. *Nature*,
Mevissen TET, Komander D, 2017. Mechanisms of deubiquitinase specificity and regulation. *Annual Review of Biochemistry*, 86(Volume 86, 2017):159–192 %U https://www.annualreviews.org/content/journals/110.1146/annurev–biochem–061516–044916.
Mistry J, Chuguransky S, Williams L, et al., 2021. Pfam: The protein families database in 2021. *Nucleic Acids Research*, 49(D1):D412–D419 %U https://doi.org/410.1093/nar/gkaa1913.
Mizzen CA, Yang X-J, Kokubo T, et al., 1996. The tafii250 subunit of tfiid has histone acetyltransferase activity. *Cell*, 87(7):1261–1270 %U https://linkinghub.elsevier.com/retrieve/pii/S0092867400818218.
Newton K, Strasser A, Kayagaki N, et al., 2024. Cell death. *Cell*, 187(2):235–256 %U https://www.sciencedirect.com/science/article/pii/S0092867423013326.
Oh HR, An CH, Yoo NJ, et al., 2017. Frameshift mutations in the mononucleotide repeats of taf1 and taf1l genes in gastric and colorectal cancers with regional heterogeneity. *Pathology oncology research: POR*, 23(1):125–130.
Pham AD, 2000. Ubiquitin-activating/conjugating activity of tafii250, a mediator of activation of gene expression in drosophila. *Science*, 289(5488):2357–2360 %U https://www.sciencemag.org/lookup/doi/2310.1126/science.2289.5488.2357.
Puglisi R, Maccari I, Pipolo S, et al., 2012. The nuclear form of glutathione peroxidase 4 is associated with sperm nuclear matrix and is required for proper paternal chromatin decondensation at fertilization. *Journal of Cellular Physiology*, 227(4):1420–1427 %U https://onlinelibrary.wiley.com/doi/abs/1410.1002/jcp.22857.
Qian B, Che L, Du Z-B, et al., 2023. Protein phosphatase 2a-b55β mediated mitochondrial p-gpx4 dephosphorylation promoted sorafenib-induced ferroptosis in hepatocellular carcinoma via regulating p53 retrograde signaling. *Theranostics*, 13(12):4288–4302 %U https://www.thno.org/v4213p4288.htm.
Ribeiro JR, Lovasco LA, Vanderhyden BC, et al., 2014. Targeting tbp-associated factors in ovarian cancer. *Frontiers in Oncology*, 4 %U https://www.frontiersin.org/journals/oncology/articles/10.3389/fonc.2014.00045/full
Roh J-L, Kim EH, Jang HJ, et al., 2016. Induction of ferroptotic cell death for overcoming cisplatin resistance of head and neck cancer. *Cancer Letters*, 381(1):96–103.
Roh J-L, Kim EH, Jang H, et al., 2017. Nrf2 inhibition reverses the resistance of cisplatin-resistant head and neck cancer cells to artesunate-induced ferroptosis. *Redox Biology*, 11:254–262 %U https://www.sciencedirect.com/science/article/pii/S2213231716303731.
Sato M, Kusumi R, Hamashima S, et al., 2018. The ferroptosis inducer erastin irreversibly inhibits system xc- and synergizes with cisplatin to increase cisplatin's cytotoxicity in cancer cells. *Scientific Reports*, 8(1):968.
Schober P, Boer C, Schwarte LA, 2018. Correlation coefficients: Appropriate use and interpretation. *Anesthesia & Analgesia*, 126(5):1763–1768 %* http://creativecommons.org/licenses/by–nc–nd/1764.1760/ %U https://journals.lww.com/00000539–201805000–201800050.
Spies J, Waizenegger A, Barton O, et al., 2016. Nek1 regulates rad54 to orchestrate homologous recombination and replication fork stability. *Molecular Cell*, 62(6):903–917 %U https://www.sciencedirect.com/science/article/pii/S1097276516301083.
Su Z, Kon N, Yi J, et al., 2023. Specific regulation of bach1 by the hotspot mutant p53r175h reveals a distinct gain-of-function mechanism. *Nature Cancer*, 4(4):564–581 %* 2023 The Author(s), under exclusive licence to Springer Nature America, Inc. %U https://www.nature.com/articles/s43018–43023–00532–z.
Sun X, Niu X, Chen R, et al., 2016. Metallothionein-1g facilitates sorafenib resistance through inhibition of ferroptosis. *Hepatology (Baltimore, Md)*, 64(2):488–500.
Sun X, Zhang Q, Lin X, et al., 2023. Imatinib induces ferroptosis in gastrointestinal stromal tumors by promoting

Unedited

stub1-mediated gpx4 ubiquitination. *Cell Death & Disease*, 14(12):1–15 %* 2023 The Author(s) %U https://www.nature.com/articles/s41419–41023–06300–41412.

Tavassoli P, Wafa LA, Cheng H, et al., 2010. Taf1 differentially enhances androgen receptor transcriptional activity via its n-terminal kinase and ubiquitin-activating and -conjugating domains. *Molecular Endocrinology*, 24(4):696–708 %U https://doi.org/610.1210/me.2009–0229.

Tong J, Li D, Meng H, et al., 2022. Targeting a novel inducible gpx4 alternative isoform to alleviate ferroptosis and treat metabolic-associated fatty liver disease. *Acta Pharmaceutica Sinica B*, 12(9):3650–3666 %U https://www.sciencedirect.com/science/article/pii/S2211383522000533.

Wang H, Curran EC, Hinds TR, et al., 2014. Crystal structure of a taf1-taf7 complex in human transcription factor iid reveals a promoter binding module. *Cell Research*, 24(12):1433–1444 %* 2014 Shanghai Institutes for Biological Sciences, Chinese Academy of Sciences %U https://www.nature.com/articles/cr2014148.

Wang H, Qi W, Zou C, et al., 2021. Nek1-mediated retromer trafficking promotes blood–brain barrier integrity by regulating glucose metabolism and ripk1 activation. *Nature Communications*, 12(1):4826 %* 2021 The Author(s) %U https://www.nature.com/articles/s41467–41021–25157–41467.

Wang R, Song S, Harada K, et al., 2020. Multiplex profiling of peritoneal metastases from gastric adenocarcinoma identified novel targets and molecular subtypes that predict treatment response. *Gut*, 69(1):18–31 %U https://gut.bmj.com/lookup/doi/10.1136/gutjnl–2018–318070.

Wang W, Liu Y, Wang Z, et al., 2024. Exploring and validating the necroptotic gene regulation and related lncrna mechanisms in colon adenocarcinoma based on multi-dimensional data. *Scientific Reports*, 14(1):22251 %U https://www.nature.com/articles/s41598–22024–73168–22253.

Wang Z, Xia Y, Wang Y, et al., 2023. The e3 ligase trim26 suppresses ferroptosis through catalyzing k63-linked ubiquitination of gpx4 in glioma. *Cell Death & Disease*, 14(10):1–13 %* 2023 The Author(s) %U https://www.nature.com/articles/s41419–41023–06222–z.

Wu Z, Geng Y, Lu X, et al., 2019. Chaperone-mediated autophagy is involved in the execution of ferroptosis. *Proceedings of the National Academy of Sciences*, 116(8):2996–3005 %* © 2019 . https://www.pnas.org/site/aboutpnas/licenses.xhtmlPublished under the PNAS license. %U https://www.pnas.org/content/2116/2998/2996.

Xie X, Chen C, Wang C, et al., 2024. Targeting gpx4-mediated ferroptosis protection sensitizes brca1-deficient cancer cells to parp inhibitors. *Redox Biology*, 76:103350 %U https://www.sciencedirect.com/science/article/pii/S2213231724003288.

Xie Y, Kang R, Klionsky DJ, et al., 2023. Gpx4 in cell death, autophagy, and disease. *Autophagy*, 19(10):2621–2638 %U https://doi.org/2610.1080/15548627.15542023.12218764.

Xu Y, Man N, Karl D, et al., 2019. Taf1 plays a critical role in aml1-eto driven leukemogenesis. *Nature Communications*, 10(1):4925 %U http://www.nature.com/articles/s41467–41019–12735–z.

Xue Q, Yan D, Chen X, et al., 2023. Copper-dependent autophagic degradation of gpx4 drives ferroptosis. *Autophagy*, 0(0):1–15 %U https://doi.org/10.1080/15548627.15542023.12165323.

Yan B, Ai Y, Sun Q, et al., 2021. Membrane damage during ferroptosis is caused by oxidation of phospholipids catalyzed by the oxidoreductases por and cyb5r1. *Molecular Cell*, 81(2):355–369.e310 %U https://www.sciencedirect.com/science/article/pii/S1097276520308029.

Yang L, Song T, Cheng Q, et al., 2019. Mutant p53 sequestration of the mdm2 acidic domain inhibits e3 ligase activity. *Molecular and Cellular Biology*, 39(4):e00375–00318 %U https://doi.org/00310.01128/MCB.00375–00318.

Yang Wan s, Sriramaratnam R, Welsch Matthew e, et al., 2014. Regulation of ferroptotic cancer cell death by gpx4. *Cell*, 156(1-2):317–331 %U https://linkinghub.elsevier.com/retrieve/pii/S0092867413015444.

Yang WS, Kim KJ, Gaschler MM, et al., 2016. Peroxidation of polyunsaturated fatty acids by lipoxygenases drives ferroptosis. *Proceedings of the National Academy of Sciences*, 113(34 %U https://pnas.org/doi/full/10.1073/pnas.1603244113)

Zhang J, Li R, Zhang B, et al., 2022. Taf1 promotes nsclc cell epithelial-mesenchymal transition by transcriptionally activating tgfβ1. *Biochemical and Biophysical Research Communications*, 636:113–118 %U https://linkinghub.elsevier.com/retrieve/pii/S0006291X22015182.

Zhang S, Zhong J, Guo D, et al., 2023. Miat shuttled by tumor-secreted exosomes promotes paclitaxel resistance in esophageal cancer cells by activating the taf1/srebf1 axis. *Journal of Biochemical and Molecular Toxicology*, 37(8):e23380 %* © 22023 Wiley Periodicals LLC. %U https://onlinelibrary.wiley.com/doi/abs/23310.21002/jbt.23380.

Zhou L, Yao Q, Ma L, et al., 2021. Taf1 inhibitor bay-299 induces cell death in acute myeloid leukemia. *Translational Cancer Research*, 10(12 %U https://tcr.amegroups.com/article/view/59486)

Unedited

Supplementary information:
Figs. S1-S5;

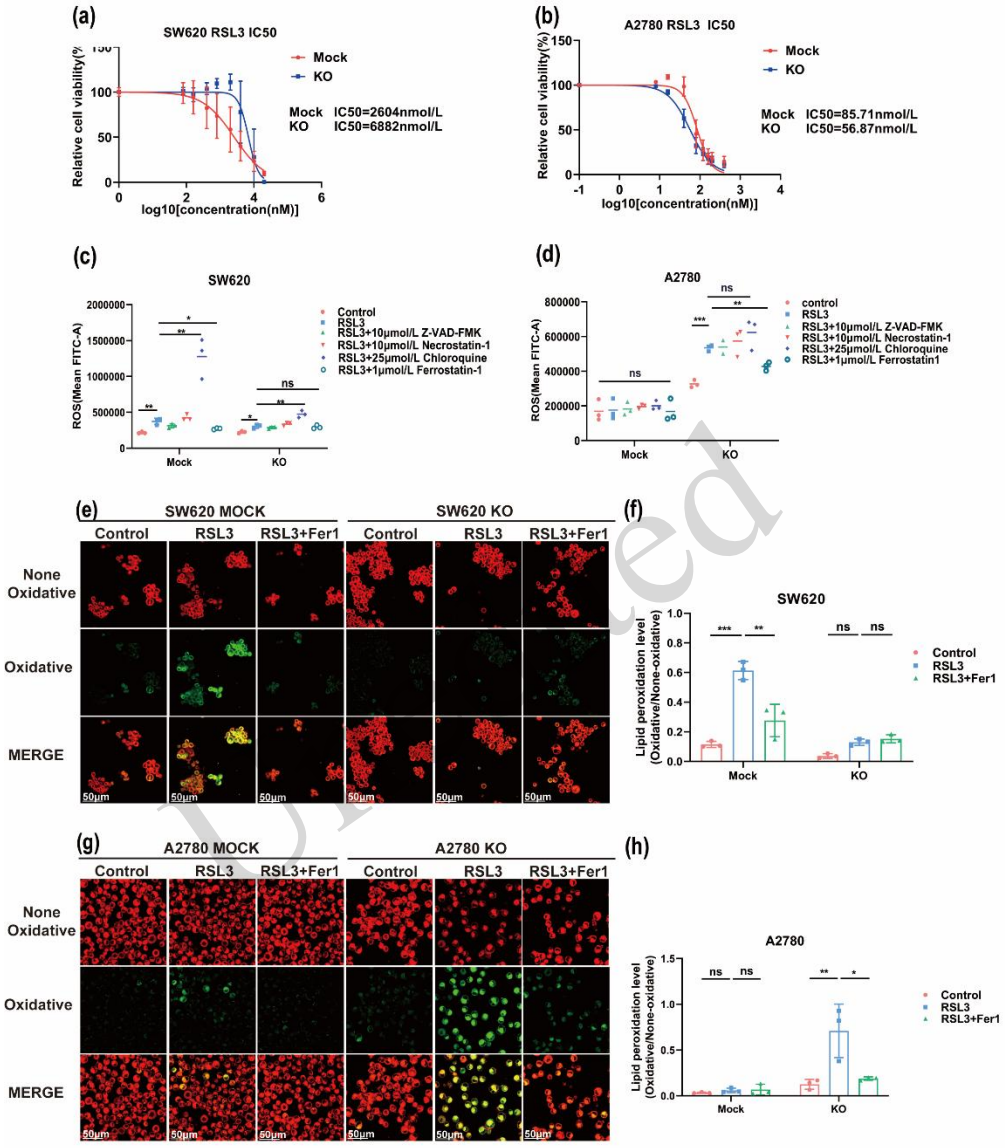

Supplement Figure 1

Fig. S1 Validation of ferroptosis in A2780 and SW620 cells

(a) Cell viability of SW620 TAF1-Mock and TAF1-KO cells treated with RSL3 for 48 h at the indicated concentrations. (b) Cell viability of A2780 TAF1-Mock and TAF1-KO cells treated with RSL3 for 48 h at the indicated concentrations. (c) Intracellular ROS levels in SW620 TAF1-Mock and TAF1-KO cells treated with 2.5μmol/L RSL3 for 48 h in the absence or presence of Z-VAD-FMK, necrostatin-1, chloroquine, or ferrostatin-1. (d) Intracellular ROS levels in A2780 TAF1-Mock and TAF1-KO cells treated with 40 nmol/L RSL3 for 24 h in the absence or presence of Z-VAD-FMK, necrostatin-1, chloroquine, or ferrostatin-1. (e, f) Representative images and quantitative analysis of LPO levels in SW620 TAF1-Mock and TAF1-KO cells

treated with 2.5μmol/L RSL3 for 48 h, with or without ferrostatin-1. (g, h) Representative images and quantitative analysis of LPO levels in A2780 TAF1-Mock and TAF1-KO cells treated with 40 nmol/L RSL3 for 24 h, with or without ferrostatin-1. All experiments were performed in triplicate. Data were presented as the mean ± SD (a, b, f and h) or as the mean (c and d). $^{*}P < 0.05$; $^{**}P < 0.01$; $^{***}P < 0.001$; not statistically significant (ns), $P > 0.05$; paired Student's t tests (c and d), one-way ANOVA (f and h).

Unedited

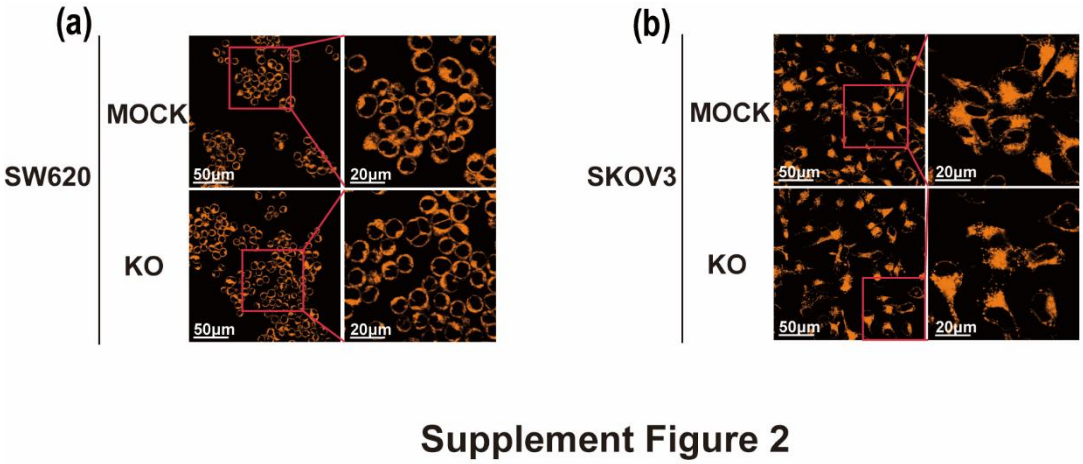

Fig. S2 Intracellular Fe^{2+} in p53-mut cells

(a) Immunofluorescence detection of intracellular Fe^{2+} in SW620 TAF1-Mock and TAF1-KO cells. (b) Immunofluorescence detection of intracellular Fe^{2+} in SKOV3 TAF1-Mock and TAF1-KO cells. All experiments were performed in triplicate.

Unedited

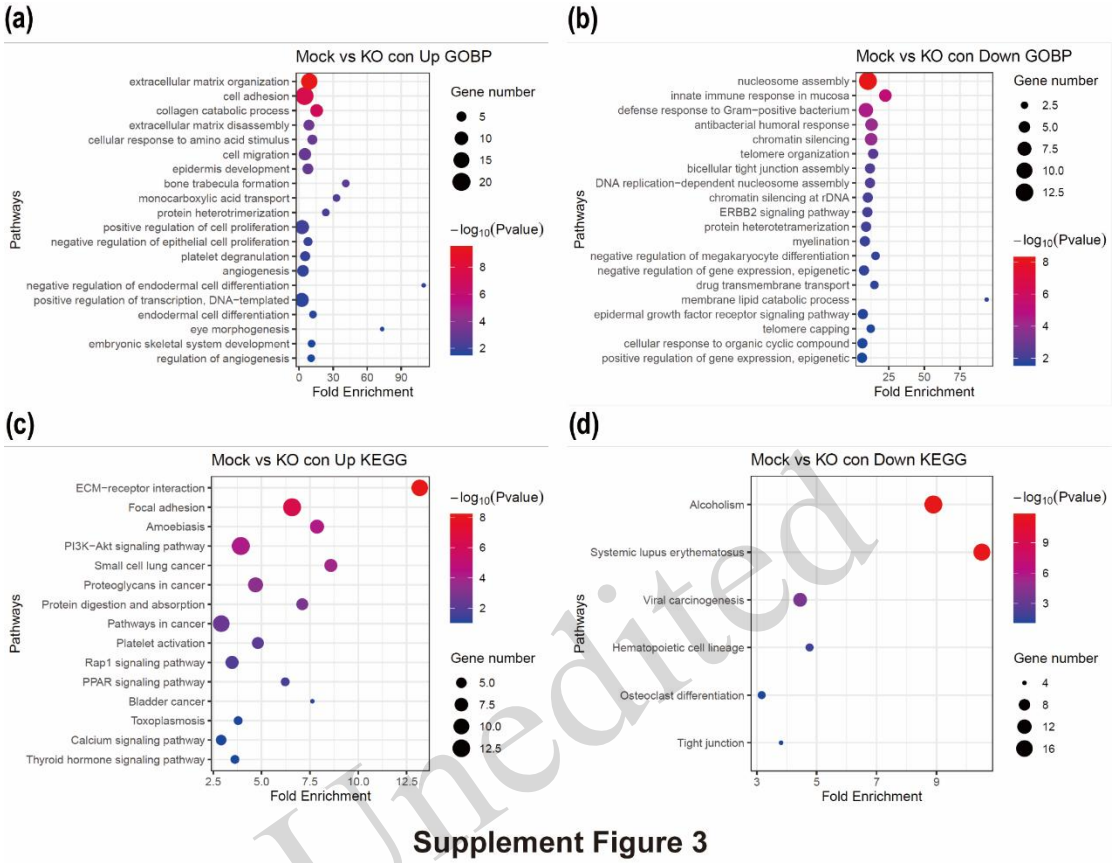

Unedited

Fig. S3 KEGG and GO pathway enrichment analysis

(a) Top 20 upregulated GO pathways in SKOV3 TAF1-Mock cells compared with TAF1-KO cells. (b) Top 20 downregulated GO pathways in SKOV3 TAF1-Mock cells compared with TAF1-KO cells. (c) Top 15 upregulated KEGG pathways in SKOV3 TAF1-Mock cells compared with TAF1-KO cells. (d) Top downregulated KEGG pathways in SKOV3 TAF1-Mock cells compared with TAF1-KO cells.

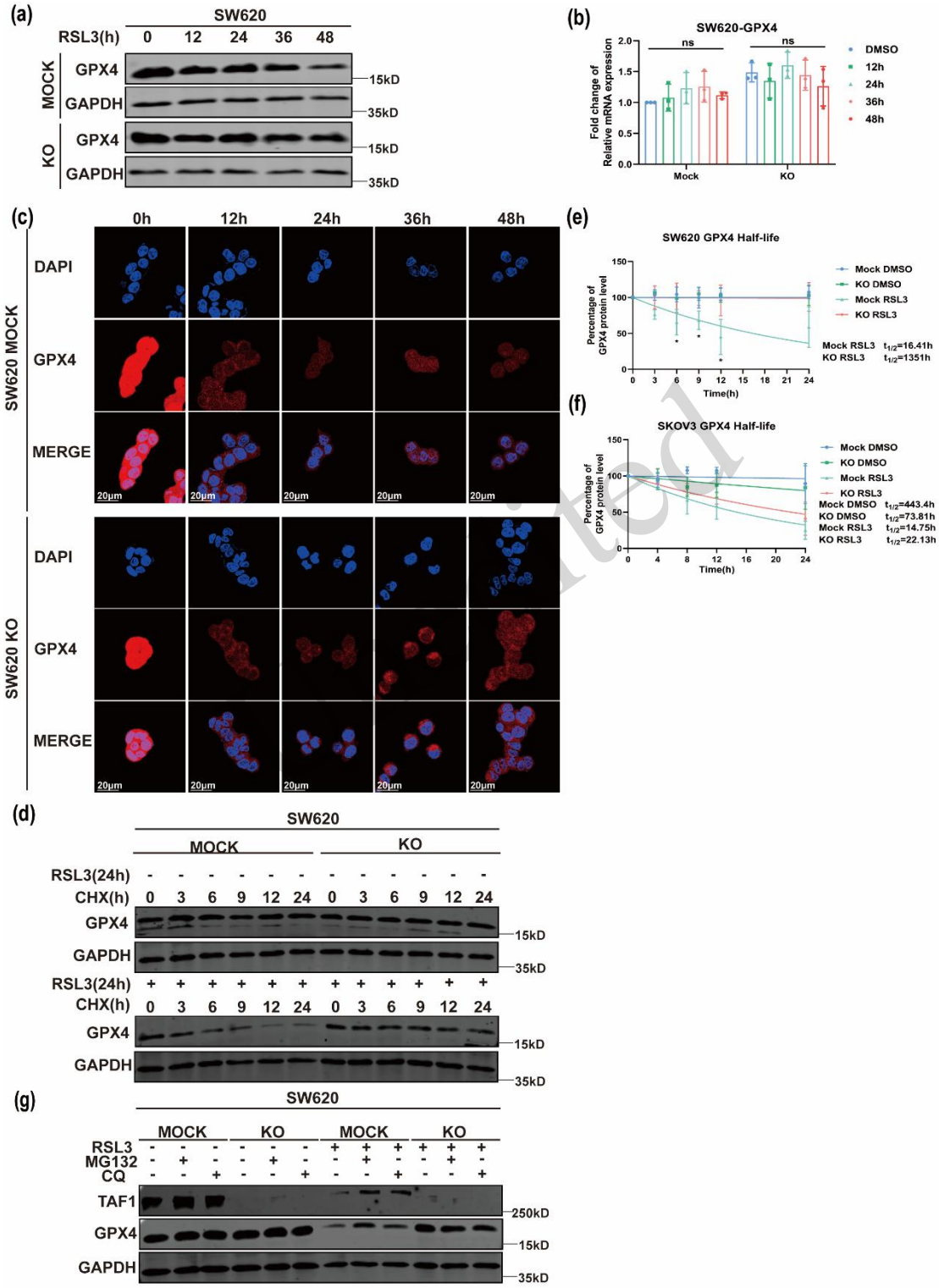

Fig. S4 TAF1-mediated degradation of nGPX4 in SW620 cells

(a) Western blot analysis of GPX4 in SW620 TAF1-Mock and TAF1-KO cells treated with 2.5 μmol/L RSL3 for the indicated time.

(b) Fold changes in relative GPX4 mRNA levels in SW620 TAF1-Mock and TAF1-KO cells treated with 2.5 μmol/L RSL3 for the indicated time. (c) Immunofluorescence staining of GPX4 in SW620 TAF1-Mock and TAF1-KO cells treated with 2.5 μmol/L RSL3 for the indicated time. (d) Western blot analysis of GPX4 in SW620 TAF1-Mock and TAF1-KO cells treated with 2.5 μmol/L RSL3 for 24 h, followed by incubation with 50 μg/mL CHX for the indicated durations. Cells were collected at the indicated time points for protein analysis. (e) CHX chase assay of GPX4 in SW620 TAF1-Mock and TAF1-KO cells. Relative protein levels were normalized to GAPDH. Related to Fig. S3d. (f) CHX chase assay of GPX4 in SKOV3 TAF1-Mock and TAF1-KO cells. Relative protein levels were normalized to GAPDH. Related to Fig. 4e. (g) Western blot analysis of GPX4 in SW620 TAF1-Mock and TAF1-KO cells treated with 2.5 μmol/L RSL3 for 48 h, followed by 10 μmol/L MG132 or 25 μmol/L CQ for 6 h. All experiments were performed in triplicate, and data are presented as mean ± SD (b, e and f). $^{*}P < 0.05$; $^{**}P < 0.01$; $^{***}P < 0.001$; ns, $P > 0.05$; one-way ANOVA (b, e and f).

Unedited

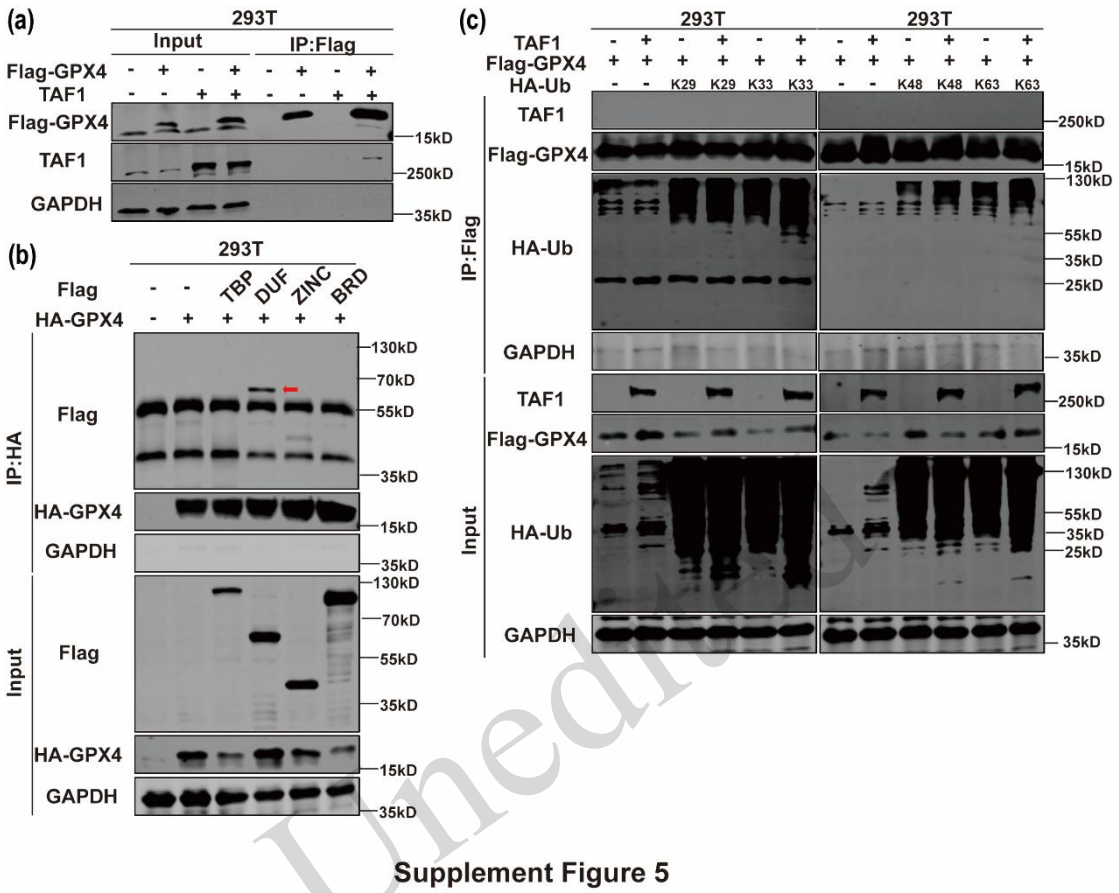

Supplement Figure 5

Fig. S5 Interaction between GPX4 and TAF1

(a) Western blot analysis of immunoprecipitated exogenous FLAG-tagged GPX4 and GFP-tagged TAF1 in HEK293T cells. (b) Western blot analysis of immunoprecipitated HA-tagged GPX4 and exogenous FLAG-tagged TAF1 truncations in HEK293T cells. (c) HEK293T cells were co-transfected with GFP-TAF1 and FLAG-GPX4 together with different ubiquitin mutants. After treatment with MG132 (10 μmol/L) for 4 h, the cells were collected and subjected to immunoprecipitation and western blot analysis. All experiments were performed in triplicate.

Unedited